Check for updates

Luminescent ruffled iridium(III) porphyrin complexes containing N-heterocyclic carbene ligands: structures, spectroscopies and potent antitumor activities under dark and light irradiation conditions†

Tsz-Lung Lam, [a] Ka-Chung Tong, [a] Chen Yang, [ab] Wai-Lun Kwong, [a] Xiangguo Guan, [ab] Ming-De Li, [a] Vanessa Kar-Yan Lo, [a] Sharon Lai-Fung Chan, ‡[c] David Lee Phillips, [a] Chun-Nam Lok*[a] and Chi-Ming Che*[ab]

A panel of iridium(III) porphyrin complexes containing axial N-heterocyclic carbene (NHC) ligand(s) were synthesized and characterized. X-ray crystal structures of the bis-NHC complexes [Ir^{III}(ttp)(IMe)$_2$]$^+$ (**2a**), [Ir^{III}(oep)(BIMe)$_2$]$^+$ (**2d**), [Ir^{III}(oep)(I^{i}Pr)$_2$]$^+$ (**2e**) and [Ir^{III}(F$_{20}$tpp)(IMe)$_2$]$^+$ (**2f**) display ruffled porphyrin rings with mesocarbon displacements of 0.483–0.594 Å and long Ir–C$_{NHC}$ bonds of 2.100–2.152 Å. Variable-temperature ^{1}H NMR analysis of **2a** reveals that the macrocycle porphyrin ring inversion takes place in solution with an activation barrier of 40 ± 1 kJ mol^{-1}. The UV-vis absorption spectra of Ir^{III}(por)–NHC complexes display split Soret bands. TD-DFT calculations and resonance Raman experiments show that the higher-energy Soret band is derived from the ^{1}MLCT dπ(Ir) → π*(por) transition. The near-infrared phosphorescence of Ir^{III}(por)–NHC complexes from the porphyrin-based $^3(\pi, \pi$*) state features broad emission bands at 701–754 nm with low emission quantum yields and short lifetimes (Φ_{em} < 0.01; τ < 4 μs). [Ir^{III}(por)(IMe)$_2$]$^+$ complexes (por = ttp and oep) are efficient photosensitizers for ^{1}O$_2$ generation (Φ_{so} = 0.64 and 0.88) and are catalytically active in the light-induced aerobic oxidation of secondary amines and arylboronic acid. The bis-NHC complexes exhibit potent dark cytotoxicity towards a panel of cancer cells with IC$_{50}$ values at submicromolar levels. The cytotoxicity of these complexes could be further enhanced upon light irradiation with IC$_{50}$ values as low as nanomolar levels in association with the light-induced generation of reactive oxygen species (ROS). Bioimaging of [Ir^{III}(oep)(IMe)$_2$]$^+$ (**2c**) treated cells indicates that this Ir complex mainly targets the endoplasmic reticulum. [Ir^{III}(oep)(IMe)$_2$]$^+$ catalyzes the photoinduced generation of singlet oxygen and triggers protein oxidation, cell cycle arrest, apoptosis and the inhibition of angiogenesis. It also causes pronounced photoinduced inhibition of tumor growth in a mouse model of human cancer.

Introduction

The recent years have witnessed a bloom in the applications of metal–N-heterocyclic carbene (NHC) complexes in catalysis,[1] materials science[2] and medicine.[3] These burgeoning research activities have benefited greatly from improved knowledge regarding the coordination chemistry of metal–NHC complexes.[4] Nonetheless, there are only a handful of examples of metalloporphyrins bearing NHC ligand(s) thus far. In this regard, the groups of Albrecht,[5] Woo[6] and Che[7] have contributed to the synthesis and investigation of the spectroscopic properties and/or catalytic activities of d^6 metalloporphyrin complexes of Co^{III}, Rh^{III}, Ir^{III} and Ru^{II} ions bearing axial NHC ligand(s). Several characteristics of these metalloporphyrins have been noted, including (1) gentle dearomatization of the porphyrin ligand; (2) elongation of the axial metal–ligand bond *trans* to the NHC ligand; and (3) pronounced ruffling of the porphyrin ligand scaffold.[5,6] The last feature, namely, NHC-induced ruffling deformation, is particularly intriguing because the out-of-plane deformation of metalloporphyrin is recognized to have a profound impact on its photophysical (*e.g.*,

electronic absorption, emission, excited state dynamics) and physiochemical properties (*e.g.*, axial ligand affinity, electron transfer rate), both of which have important implications in biological processes involving the ubiquitous tetrapyrrole compounds.[8] While many studies on nonplanar metalloporphyrins have focused on metal ions of relatively small size, such as Ni^{II}[8a,9] and Zn^{II},[10] and those with Mn^{III}[11] and Fe^{III},[12] in which nonplanarity is primarily induced by the peripheral substituents of the porphyrin, fewer studies have been performed on axial ligand-induced porphyrin ring deformation in d^6 metalloporphyrins.[5,6,13]

The Soret and Q bands in the electronic absorption spectra of metalloporphyrins of d^6 Ru^{II}, Os^{II}, Rh^{III} and Ir^{III} generally display marked hypsochromic shifts with respect to their free base porphyrins due to $d\pi(M)–\pi^*(por)$ interaction.[14] Axial ligand(s) can also perturb the absorption spectra by modulating the electronic properties of the metal ion and hence the metal–porphyrin bonding interaction (*cis*-effect).[14] The literature reports that d^6 metalloporphyrins display red to infrared phosphorescence derived from the $^3(\pi, \pi^*)$ IL state of the porphyrin ligand or the $^3(d\pi, \pi^*)$ metal-to-ligand charge transfer (MLCT) state upon photoexcitation.[15] Nevertheless, only Ir^{III}–porphyrin complexes emit strong red to near-infrared (NIR) phosphorescence in solution at room temperature, with emission quantum yields up to 0.30 and emission lifetimes up to 97 μs.[16a–c] Due to these advantageous luminescence properties, the use of cationic Ir^{III}-oep-derived bioconjugates for cellular imaging and as phosphorescent probes for intracellular oxygen sensing has been reported by Papkovsky and co-workers.[16b] On the other hand, two near-IR-absorbing BODIPY assemblies of Ir^{III}–porphyrin, recently reported by Shen, Chan, Mack and co-workers,[16d] have been shown to display excellent photostability and efficiency in photosensitized singlet oxygen generation with a quantum yield of up to 0.85.[16d] These encouraging findings have shed light on the potential photobiological uses of Ir^{III}–porphyrin complexes, which remain unexplored.

Here, we describe the synthesis and characterization of a panel of luminescent ruffled iridium(III) porphyrin complexes containing mono-NHC and bis-NHC ligand(s), namely, $[Ir^{III}(por)(NHC)Cl]$ (**1a–1d**) and $[Ir^{III}(por)(NHC)_2]^+$ (**2a–2f**), respectively. Steady-state and time-resolved spectroscopic studies and theoretical calculations in conjunction with resonance Raman spectroscopy were undertaken to examine the effects of NHC ligation on the photophysical properties and electronic structures of the Ir^{III}–porphyrin complexes. In addition, the photochemical reactivity *via* the light-induced generation of singlet oxygen as well as the cytotoxicity and phototoxicity of these bis-NHC iridium(III) porphyrin complexes were investigated both *in vitro* and *in vivo*.

Results

Synthesis

The reported synthetic approaches to metalloporphyrin-NHC complexes include the thermal decarboxylation of imidazolium carboxylate,[5] deprotonation of the imidazolium salt with a strong base[7] and incorporation of the free imidazoylidene.[6] In this work, the coordination of NHC ligands to iridium(III)

porphyrin was accomplished by reacting bis(NHC)silver(I) complex[17] with $[Ir^{III}(por)Cl(CO)]$ *via* transmetalation. This synthetic protocol offers the advantage that the reaction can be conducted under mild, aerobic conditions. Mono-NHC complexes $[Ir^{III}(por)(NHC)Cl]$ (**1a–1d**) were prepared by stirring a mixture of $[Ir^{III}(por)Cl(CO)]$ with half equivalents of the respective bis(NHC)silver(I) complexes in CH_2Cl_2 at room temperature for 12 h (Scheme 1). After the removal of AgCl salt by filtration through a short plug of Celite (when por = tmp, where H_2tmp = *meso*-tetramesitylporphyrin) or a silica gel column (when por = F_{20}tpp, where H_2F_{20}tpp = *meso*-tetrakis(pentafluorophenyl)porphyrin), the desired complexes were recrystallized from CH_2Cl_2/hexane and obtained in 60–74% isolated yields. Bis-NHC complexes **2a–2f** were similarly synthesized by reacting stoichiometric amounts of bis(NHC)silver(I) complexes with $[Ir^{III}(por)Cl(CO)]$ in CH_2Cl_2 at room temperature or at 40 °C for 12 h to 4 days (Scheme 2). The complexes were then purified by flash column chromatography on a silica gel column using CH_2Cl_2/EtOAc as the eluent and were obtained in 70–96% isolated yields. $[Ir^{III}(oep)(CNPhOMe)_2]^+$ (**3**) and $[Ir^{III}(oep)(py)_2]^+$ (**4**) were also prepared for comparative study (see ESI†).

The number of coordinated NHC ligands was revealed by the ^1H NMR and FAB-MS analyses of the complexes and is dependent on the steric bulk of the porphyrin ligand. Specifically, whereas
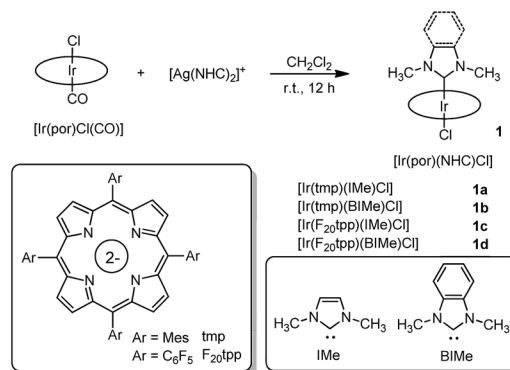
Scheme 1 Synthesis of $[Ir^{III}(por)(NHC)Cl]$ complexes **1a–1d**.
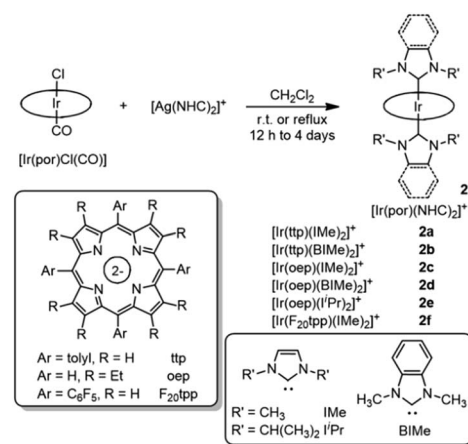
Scheme 2 Synthesis of $[Ir^{III}(por)(NHC)_2]^+$ complexes **2a–2f**.

a 1 : 1 bis(NHC)silver(ɪ) complex with $[Ir^{III}(por)Cl(CO)]$ (por = ttp or oep) recipe gave solely $[Ir^{III}(por)(NHC)_2]^+$ complexes, the same stoichiometry furnished only $[Ir^{III}(tmp)(NHC)Cl]$ and trace $[Ir^{III}(tmp)(NHC)]^+$ complexes in the case of $[Ir^{III}(tmp)Cl(CO)]$. The reaction of bis(NHC)silver(ɪ) complex with $[Ir^{III}(F_{20}tpp)Cl(CO)]$ to give $[Ir^{III}(F_{20}tpp)(IMe)_2]^+$ (**2f**) was completed at elevated temperature with extended reaction time (refluxing CH_2Cl_2 for 4 days). The FAB-MS spectra of complexes **1a–1d** all show peaks attributed to $[M - Cl]^+$ fragments, suggesting that the Ir–Cl bond is weakened by the *trans*-axial NHC ligand. The IR oxidation-state marker bands of all complexes **1a–1d** and **2a–2f** fall into the range of 1018–1022 cm^{-1}, which is comparable to that of their parental complexes $[Ir^{III}(por)Cl(CO)]$ and consistent with the iridium(ɪɪɪ) oxidation state.[18] Mono-NHC complexes **1a**, **1b** and **1d** are stable in the solid state and in CDCl$_3$ solution for 1 week with the exception of **1c**, which decomposes within 1 day under ambient conditions. Bis-NHC complexes **2a–2e** are remarkably air-stable in the solid state and in CDCl$_3$ solution in the dark for 1 month, as revealed by ^1H NMR spectroscopy and UV-vis absorption spectroscopy, except for **2f**, which gradually deteriorates in CDCl$_3$ in 3 days.

X-ray crystal structures

The structures of **2a**, **2d**, **2e** and **2f** were determined by X-ray diffraction analysis, and their perspective views are depicted in Fig. 1. Selected bond distances and angles are summarized in Table 1. All complexes adopt a slightly distorted octahedral geometry, with the porphyrin ring exhibiting a significant ruffling deformation. The mean deviations of the mesocarbon atom from the least square plane of the porphyrin ring in **2a**, **2d**, **2e** and **2f** are 0.483, 0.557, 0.561 and 0.594 Å, respectively. The

Table 1 Selected bond lengths (Å) and bond angles (°) of **2a**, **2d**, **2e** and **2f**

	2a	2d	2e	2f
Ir–C$_{NHC1}$	2.140(17)	2.128(3)	2.151(5)	2.080(3)
Ir–C$_{NHC2}$	2.164(18)	2.128(3)	2.143(5)	2.120(3)
Ir–N$_{mean}^a$	2.027(11)	2.023(3)	2.147(16)	1.985(17)
C$_{NHC1}$–Ir–C$_{NHC2}$	177.9(16)	177.62(15)	179.4(16)	174.5(10)

^{a} Ir–N$_{mean}$ is the average bond distance of four Ir–N$_{por}$ bonds.

planes of the NHC ligands are slightly to moderately tilted with respect to the Ir–C$_{NHC}$ axis. The mean pitch angles of the NHC ligands (measurement of out-of-plane tilting) of **2a**, **2d**, **2e** and **2f** are 7.5°, 4.6°, 1.4° and 5.1° respectively. The pitch angle of **2a** is slightly larger than that of $[Ir^{III}(ttp)(IBuMe)Me]$ (6.4°).[6] The ruffling deformation of the porphyrin ring combined with the tilting of NHC ligands is considered to be a means to relieve the unfavorable steric repulsion caused by the close proximity of the NHC ligands and porphyrin ring. Ruffling deformation of porphyrin rings has also been observed in other NHC-bearing metalloporphyrin complexes.[5,6] In all the X-ray crystal structures, the planes of the NHC ligands are approximately orthogonal to each other, with an interplanar angle of 84.8° for **2a**, 69.2° for **2d**, 87.7° for **2e** and 80.9° for **2f**. The orientation of NHC ligands with respect to Ir–N$_{por}$, described by the torsional angle of N$_{NHC}$–C$_{NHC}$–Ir–N$_{por}$, has an average value of 40.3° for **2a**, 35.0° for **2d**, 43.5° for **2e** and 37.0° for **2f**. The near-staggered orientation of the NHC ligands with respect to Ir–N$_{por}$ suggests minimal Ir–C$_{NHC}$ π bonding interaction.[5a] Evidently, the arrangement of NHC ligands is related to the structural requirement for ruffling deformation of porphyrin ligands.
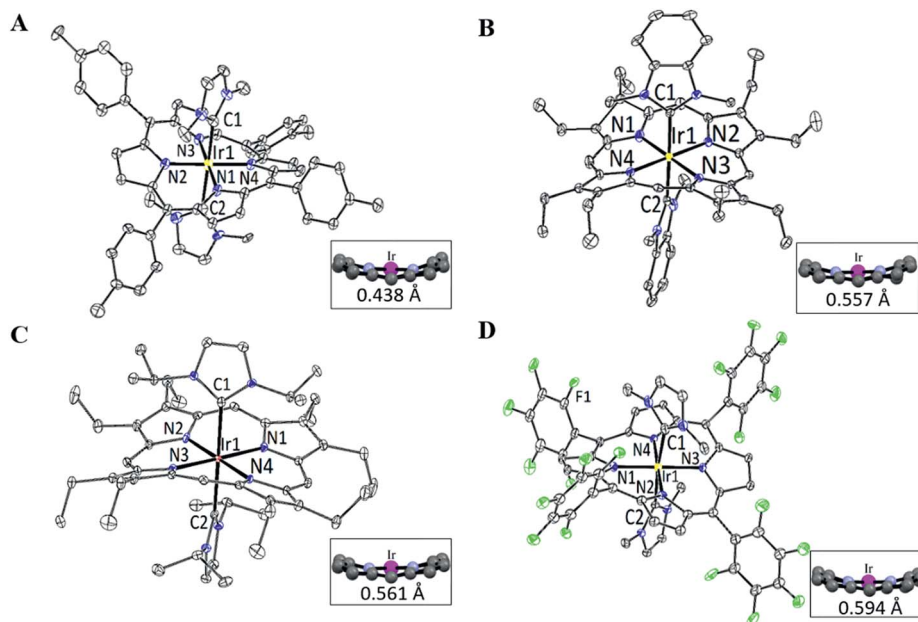
Fig. 1 Perspective views of (A) $[Ir^{III}(ttp)(IMe)_2]^+$ **2a**, (B) $[Ir^{III}(oep)(BIMe)_2]^+$ **2d**, (C) $[Ir^{III}(oep)(I^iPr)_2]^+$ **2e** and (D) $[Ir^{III}(F_{20}tpp)(IMe)_2]^+$ **2f** at 30% probability of the thermal ellipsoid. Hydrogen atoms, cocrystallized solvent molecules and counteranions are omitted for clarity. Insets show the side views of the porphyrin cores and the average mesocarbon displacements (Å) from the mean porphyrin planes.

The average Ir–N distances of **2a**, **2d**, **2e** and **2f** are 2.027, 2.023, 2.017 and 1.985 Å, respectively, which are comparable to those of other organoiridium(III) porphyrin complexes.[16,19] The mean Ir–C_{NHC} distances of **2a**, **2d**, **2e** and **2f** are 2.152, 2.128, 2.147 and 2.100 Å, respectively, which are longer than those of non-porphyrin-type Ir–NHC complexes reported in the literature.[20] The elongated Ir–C_{NHC} bond in the $[Ir^{III}(por)(NHC)_2]^+$ complexes is a consequence of the combination of (1) the strong *trans* influence of the NHC ligands and (2) the unfavorable steric interactions between the *N*-alkyl substituents on the NHC ligands and the porphyrin ring. While the influence of the *N*-alkyl groups of the NHC ligand on the Ir–C_{NHC} distance is marginal (*cf.* **2d** *vs.* **2e**), the change of the porphyrin from tpp to F_{20}tpp ligand reduces the Ir–C_{NHC} distance by 0.052 Å (*cf.* **2a** *vs.* **2f**). In comparison, the Ir–C_{NHC} distances in $[Ir^{III}(ttp)(IMe)_2]^+$ (**2a**) are discernibly shorter than that reported in $[Ir^{III}(ttp)(IBuMe)Me]$ (2.194(4)Å).[6] This finding indicates that the methyl ligand has a stronger *trans* influence than NHC. In addition, the extensive intermolecular π–π stacking interactions between the molecules of **2d** to form 1D polymeric chains are worth noting (Fig. 2A). The neighboring BIMe ligands are parallel to one another with an interplanar angle of 0° and a short interplanar distance of 3.398 Å. Intriguingly, the intermolecular interactions have presumably led to the self-assembled fibrous structure of **2d** observed by TEM upon precipitating the complex in a THF/H$_2$O (1 : 90, v/v) mixture (Fig. 2B).

NMR study

The ^{1}H NMR spectra of all $[Ir^{III}(por)(NHC)Cl]$ and $[Ir^{III}(por)(NHC)_2]^+$ complexes show upfield signals of the *N*-alkyl substituents on the NHC ligands at <0 ppm (TMS reference), revealing the anisotropic effect of the porphyrin ring current upon these alkyl groups. The static crystal structures of **2a**, **2d**, **2e**, and **2f** have two-fold symmetry due to the ruffling deformation of the porphyrin ligand. However, all iridium(III) porphyrin complexes in this work display a pseudo-four-fold symmetry in solution; both H$_\beta$ (when por = tmp, F$_{20}$tpp or ttp) and H$_{meso}$ (when por = oep) appear to be singlet.

Metalloporphyrins are known to exhibit a variety of conformational dynamics in solution, and the dynamic processes associated with porphyrin ligands include macrocyclic inversion, *meso*- and β-substituent rotation.[21] For the related $[Rh^{III}(tpp)(IMe)Cl]$ and $[M(ttp)(IBuMe)Me]$ (M = Rh^{III} or Ir^{III})

complexes, *meso*-aryl ring rotation about the C_{meso}–C_{Ar} bond was suggested to occur with the corresponding $\Delta G^{\ddagger}_{ROT}$, which measured 59–63 kJ mol^{-1}.[5b,6] In this work, the ^{1}H NMR spectra of **2a** from 298 K to 193 K were recorded (Fig. 3) to study its fluxional behavior in solution. At 298 K, the H$_o$ and H$_m$ signals of the *meso*-tolyl rings appear as two well-resolved doublets, indicating that these nuclei are at their fast exchange limits. As the temperature is lowered, the H$_o$ signal broadens and completely collapses (coalesces) at 223 K. Meanwhile, the H$_m$ signal broadens and coalesces at 208 K. At 193 K, four new sets of signals from H$_o$ and H$_m$ have developed, though they are not well resolved. Notably, the two H$_o$ signals are anomalously split by 1.4 ppm, with one of the H$_o$ signals being farther upfield than the H$_m$ signals. With reference to the related VT ^{1}H NMR study of ruffled Ni^{II}–por complexes,[9a] the observed splitting of the H$_o$ signal at the low-temperature limit reveals a situation in which half of H$_o$ lies above the shielding region of the relatively "frozen" porphyrin ring, which is in a ruffled conformation. The chemical equivalence of H$_\beta$ of ttp as well as of H$_a$ and N–Me from two IMe ligands is conserved, as these signals remain singlets throughout the experiment. Considering the symmetric bis-ligation and symmetry of the IMe ligand and the *meso*-tolyl group, the observed temperature-dependent NMR behavior of **2a** is associated with a single dynamic process in which macrocyclic inversion is preferred over axial ligand rotation or *meso*-tolyl ring rotation.[22] From the coalescence temperature and coalescence exchange rate (k_{exch}) of the H$_o$ and H$_m$ signals, the activation barrier of the ring inversion ($\Delta G^{\ddagger}_{ROT}$) of **2a** is estimated to be 40 ± 1 kJ mol^{-1}. In addition, the reversible binding of NHC ligand(s) to Ir^{III} ion is suggested not to take place at room temperature because the ^{1}H signals from the NHC ligand(s) (*i.e.*, H$_a$ and N–Me) remained unaltered

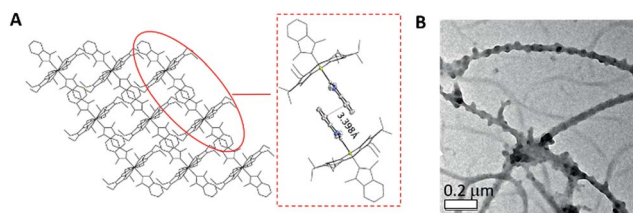Fig. 2 (A) The crystal packing diagram of **2b** viewed along the *b*-axis and an enlarged image of a pair of **2b** molecules with an interplanar distance of 3.398 Å. (B) TEM image obtained from THF/H$_2$O (1 : 90, v/v) mixture.
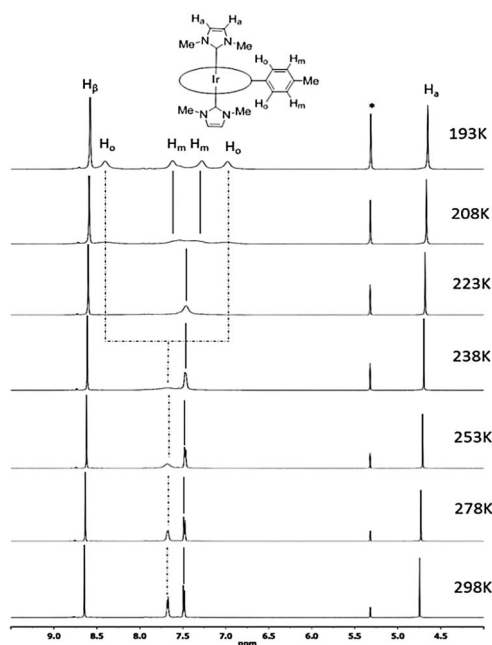

Fig. 3 Selected region of ^{1}H NMR spectra (500 MHz) of $[Ir^{III}(ttp)(IMe)_2]^+$ **2a** in CD$_2$Cl$_2$ from 298 K to 193 K. Asterisks (*) denote residual CHDCl$_2$ signal.

throughout the VT ^{1}H NMR experiment.[6] The chemical shifts of H_β and H_{meso} as well as of carbene C_{NHC} are summarized in Table 2. The chemical shift of H_β or H_{meso} is a useful parameter to assess the donor strength of the axial ligands.[15c,23] For instance, replacing a π-accepting CO ligand with a σ-donating NHC ligand in $[Ir^{III}(tmp)(L)Cl]$ and $[Ir^{III}(F_{20}tpp)(L)Cl]$ results in an upfield shift of the H_β signal by 0.30–0.43 ppm. The H_{meso} signals for the $[Ir^{III}(oep)(L)_2]^+$ complexes differ by $\sim$0.9 ppm for L = isocyanide ligand (**3**) and $\sim$0.8 ppm for L = pyridine ligand (**4**) versus L = NHC ligand (**2c–2e**). The H_β or H_{meso} signals for $[Ir^{III}(por)(NHC)Cl]$ and $[Ir^{III}(por)(NHC)_2]^+$ complexes bearing axial BIMe ligands are shifted downfield by 0.04–0.08 ppm compared to those of the IMe analogs, showing that the latter is a stronger donor. The effect of the N-alkyl substituent on the NHC ligand was found to be insignificant, as revealed by the H_{meso} signals of **2c** and **2e**.

Electrochemistry

The electrochemical data and cyclic voltammograms of complexes **2a**, **2e** and **2f** are displayed in Table 3 and Fig. 4, respectively. The quasireversible/irreversible reduction waves of these complexes appear at $E_{1/2} = -1.31$–2.01 V (vs. Ag/AgNO$_3$). The first reversible oxidation couple occurs at $E_{1/2} = +0.51$–+1.12 V, while the second quasireversible/irreversible oxidation takes place at $E_{1/2} = +1.15$–+1.45 V. To identify the site of the first oxidation and reduction of **2a**, the spectroelectrochemistry was studied. The UV-vis absorption spectra of **2a** recorded at various time intervals in the first oxidation and reduction display similar spectral characteristics; the intensity of the Soret bands decrease considerably with the concomitant development of a broad IR-range absorption in the Q bands, ca. 700–1000 nm (Fig. 5). These spectral features are typical of the π-radical cation or anion of the porphyrin ring.[24] On the other hand, the $E_{ox} - E_{red}$ values for the first oxidation and first reduction of the $[Ir^{III}(por)(NHC)Cl]$ and $[Ir^{III}(por)(NHC)_2]^+$

Table 3 Electrochemical data of **1–4**^{a}

Complex		E_{red} (V)	E_{ox} (V)	$E_{ox} - E_{red}^c$ (V)
$[Ir^{III}(tmp)(IMe)Cl]$	**1a**	−1.91	+0.51, +1.15	2.42
$[Ir^{III}(tmp)(BIMe)Cl]$	**1b**	−1.87	+0.54, +1.19	2.41
$[Ir^{III}(F_{20}tpp)(BIMe)Cl]$	**1d**	−1.31	+1.12, +1.39	2.43
$[Ir^{III}(ttp)(IMe)_2]^+$	**2a**	−1.60	+0.73, +1.37^b	2.33
$[Ir^{III}(ttp)(BIMe)_2]^+$	**2b**	−1.48	+0.85, +1.45^b	2.33
$[Ir^{III}(oep)(IMe)_2]^+$	**2c**	−1.80	+0.72, +1.25	2.52
$[Ir^{III}(oep)(BIMe)_2]^+$	**2d**	−1.78	+0.79, +1.24^b	2.57
$[Ir^{III}(oep)(I^iPr)_2]^+$	**2e**	−1.82	+0.75, +1.29	2.57
$[Ir^{III}(F_{20}tpp)(IMe)_2]^+$	**2f**	−1.77, −1.11	+1.31	2.42
$[Ir(oep)(CNPhOMe)_2]^+$	**3**	−1.86	+0.72, +1.39^b	2.58
$[Ir(oep)(py)_2]^+$	**4**	−1.81	+0.80, +1.44^b	2.61

^{a} $E_{1/2}$ (V vs. Ag/AgNO$_3$, scan rate = 100 mV s^{-1}) in CH$_2$Cl$_2$ with 0.1 M [^{n}Bu$_4$N]PF$_6$ as electrolyte at r.t.; $E_{1/2}$ (Cp$_2$Fe$^{+/0}$) = 0.14 V. ^{b} E_{pa} of irreversible wave. ^{c} Potential difference between the first oxidation and first reduction.
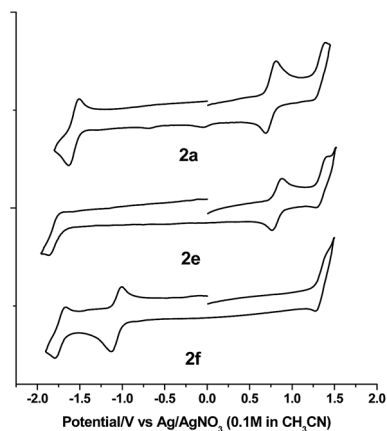

Fig. 4 Cyclic voltammograms of **2a**, **2e** and **2f** in CH$_2$Cl$_2$ (scan rate = 100 mV s^{-1}).

Fig. 5 UV-vis absorption spectral changes of **2a** containing 0.1 M [^{n}Bu$_4$N]PF$_6$ during the first oxidation (top) and first reduction (bottom). Asterisk denotes an instrumental artifact.

Table 2 Chemical shifts of H_β and H_{meso} in CDCl$_3$

Complex		$\delta H_\beta{}^a$ (ppm)	$\delta H_{meso}{}^a$ (ppm)
$[Ir^{III}(ttp)Cl(CO)]$		8.96	—
$[Ir^{III}(tmp)Cl(CO)]$		8.66	—
$[Ir^{III}(oep)Cl(CO)]$		—	10.31
$[Ir^{III}(F_{20}tpp)Cl(CO)]$		9.01	—
$[Ir^{III}(tmp)(IMe)Cl]$	**1a**	8.32	—
$[Ir^{III}(tmp)(BIMe)Cl]$	**1b**	8.36	—
$[Ir^{III}(F_{20}tpp)(IMe)Cl]$	**1c**	8.58	—
$[Ir^{III}(F_{20}tpp)(BIMe)Cl]$	**1d**	8.62	—
$[Ir^{III}(ttp)(IMe)_2]^+$	**2a**	8.61	—
$[Ir^{III}(ttp)(BIMe)_2]^+$	**2b**	8.69	—
$[Ir^{III}(oep)(IMe)_2]^+$	**2c**	—	9.39
$[Ir^{III}(oep)(BIMe)_2]^+$	**2d**	—	9.45
$[Ir^{III}(oep)(I^iPr)_2]^+$	**2e**	—	9.40
$[Ir^{III}(F_{20}tpp)(IMe)_2]^{+b}$	**2f**	8.70	—
$[Ir^{III}(oep)(CNPhOMe)_2]^+$	**3**	—	10.31
$[Ir^{III}(oep)(py)_2]^+$	**4**	—	10.21

^{a} Values reported with reference to $\delta H(Si(CH_3)_4) = 0$ ppm. ^{b} Measured in CD$_2$Cl$_2$.

complexes fall in the range of 2.33–2.61 V, which are comparable to the conventional HOMO–LUMO gap of metalloporphyrin complexes.[25] Thus, both the first oxidation and first reduction are assigned to porphyrin-center processes. The $E_{1/2}$

values for the IMe complexes (**1a**, **2a** and **2c**) are less anodic compared to the corresponding BIMe analogs (**1b**, **2b** and **2d**, respectively; Table 5). This difference suggests that IMe is a stronger donor ligand than BIMe, which is similar to the findings from the ^{1}H NMR analysis. Nonplanarity of metalloporphyrins is known to engender cathodic shift of redox potential.[9b,d,10a,26] However, the effect of ruffling on redox potential is negligible for **2c–2e** because the redox potentials of these complexes are comparable to those of the analogous bisisocyanide complex (**3**) and bis-pyridine complex (**4**), with ΔE being less than 0.08 V.

UV-visible absorption spectroscopy

The UV-visible spectral data and photophysical data of **1–4** and their parental [Ir^{III}(por)Cl(CO)] complexes are summarized in Table 4. The UV-vis absorption spectra of complexes **1a–1d**, which bear mono-NHC ligands, exhibit a moderately intense absorption band at 367–371 nm in addition to a Soret band at 431 nm (**1a** and **1b**, por = tmp) or 426 nm (**1c** and **1d**, por = F$_{20}$tpp) with one or two Q band(s) at 530–595 nm (Table 4). All bis(NHC)iridium(III) porphyrin complexes **2** display two intense Soret bands with peaks at 372–375 nm and 428–440 nm, respectively, with λ_{max} of the Q band spanning from 532 to 620 nm (Table 4). The separation of the two Soret bands of **1** and **2** is 54–66 nm. This type of absorption spectrum featuring two Soret bands is classically termed a 'hyperspectrum'.[14,15c] Fig. 6 compares a representative hyperspectrum from **2c** to 'normal' spectra from [Ir^{III}(oep)Cl(CO)], **3** and **4**. The degree of 'hyper character' can be evaluated by $\Delta \log \varepsilon$ between the two Soret bands (i.e., the larger $\Delta \log \varepsilon$, the greater the 'hyper character' is). Thus, the hyper character of the bis-NHC complexes **2** is
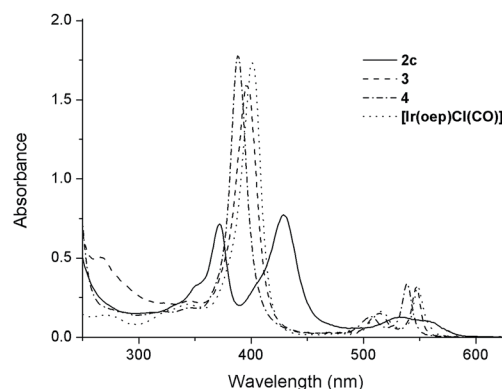

Fig. 6 UV-vis absorption spectra of **2c**, **3**, **4** and [Ir(oep)Cl(CO)] in CHCl$_3$ (1×10^{-5} M).

generally stronger than that of the mono-NHC complexes **1**. Moreover, the hyper character appears to be a function of the porphyrin ligand; $\Delta \log \varepsilon$ ranges from 0.36 for **2a** and **2b** (por = ttp) to 0.11 for **2f** (por = F$_{20}$ttp) and 0–0.06 for **2c–2e** (por = oep).

In addition to the presence of an extra Soret band, the Soret and Q bands of the NHC complexes are broadened compared to those of their parental [Ir^{III}(por)Cl(CO)]. Moreover, a sizable redshift of the low-energy Soret band is noted. For example, in the oep series, the low-energy Soret band of **2c** is redshifted by 26, 34 and 41 nm versus those of [Ir^{III}(oep)Cl(CO)], **3** and **4**, respectively. The same trend holds for the cases of **1c**, **1d** and **2f** versus their parental [Ir^{III}(F$_{20}$tpp)Cl(CO)] complex, where $\Delta \lambda_{max}$ (redshift) are 12, 12 and 26 nm, respectively (Fig. S14†).

Complexes **1b**, **1d**, **2b** and **2d**, which contain BIMe ligand(s), display an exclusive absorption of moderate intensity (log ε = 4.41–4.63) at λ_{max} = 296–301 nm, which can be attributed to π

Table 4 UV-visible absorption and emission data of [Ir^{III}(por)Cl(CO)] and **1–4**

Complex		λ_{max} nm^{-1} (log ε)	λ_{max}/nm (τ/μs)	Φ_{em} [$\times 10^{-2}$]
		UV-vis absorption data^a	Emission data^a Solution at 298 K	
[Ir^{III}(ttp)Cl(CO)]		309 (4.50), 422 (5.58), 533 (4.41), 567 (3.89)	724 (47.2), 808 (sh)	0.16
[Ir^{III}(tmp)Cl(CO)]		311 (4.43), 422 (5.58), 533 (4.42), 564 (3.60)	721 (77.2), 800 (sh)	0.22
[Ir^{III}(oep)Cl(CO)]		342 (4.44), 403 (5.38), 518 (4.30), 549 (4.62)	666 (83.3), 722 (sh)	5.03
[Ir^{III}(F$_{20}$tpp)Cl(CO)]		329 (4.40), 414 (5.42), 526 (4.45), 557 (3.94)	676 (101.0), 746 (sh)	2.92
[Ir^{III}(tmp)(IMe)Cl]	**1a**	345 (sh) (4.29), 368 (4.56), 431 (5.18), 524 (4.06), 593 (3.40)	773 (1.8)	0.05
[Ir^{III}(tmp)(BIMe)Cl]	**1b**	301 (4.55), 367 (4.61), 431 (5.23), 545 (4.13), 592 (3.92)	775 (2.3)	0.06
[Ir^{III}(F$_{20}$tpp)(IMe)Cl]	**1c**	346 (sh) (4.44), 371 (4.62), 426 (5.10), 533 (4.12)	—^{b}	—^{b}
[Ir^{III}(F$_{20}$tpp)(BIMe)Cl]	**1d**	296 (4.41), 346 (sh) (4.39), 369 (4.55), 426 (5.10), 535 (4.12)	729 (1.7), 811 (sh)	0.29
[Ir^{III}(ttp)(IMe)$_2$]$^+$	**2a**	374 (4.76), 438 (5.12), 547 (3.87), 620 (3.82) (br)^c	Nonemissive	—
[Ir^{III}(ttp)(BIMe)$_2$]$^+$	**2b**	297 (4.63), 372 (4.63), 437 (4.99), 564 (3.85) (br)^d, 611 (3.87) (br)^c	Nonemissive	—
[Ir^{III}(oep)(IMe)$_2$]$^+$	**2c**	351 (sh) (4.52), 372 (4.86), 429 (4.89), 532 (4.10), 556 (4.01)	701 (2.7), 766 (sh)	0.41
[Ir^{III}(oep)(BIMe)$_2$]$^+$	**2d**	297 (4.42), 373, (4.76), 428 (4.82), 533 (4.03), 557 (3.95)	701 (3.6), 765 (sh)	0.66
[Ir^{III}(oep)(I^{i}Pr)$_2$]$^+$	**2e**	353 (sh) (4.49), 375 (4.82), 432 (4.82), 537 (4.09), 560 (4.02)	701 (1.9), 763 (sh)	0.03
[Ir^{III}(F$_{20}$tpp)(IMe)$_2$]$^+$	**2f**^{d}	355 (sh) (4.63), 374 (4.89), 418 (sh) (4.72), 440 (5.00), 537 (4.13)	754 (0.5), 829 (sh)	0.08
[Ir^{III}(oep)(CNPhOMe)$_2$]$^+$	**3**	266 (4.70), 344(sh) (4.36), 395 (5.20), 515 (4.17), 547 (4.50)	663 (124.7), 717(sh)	6.40
[Ir^{III}(oep)(py)$_2$]$^+$	**4**	388 (5.25), 507 (4.11), 539 (4.54)	651(55.2), 711(sh)	12.30

^{a} Measurements were performed in degassed CHCl$_3$. ^{b} Complex **1d** was unstable for emission measurements. ^{c} Broad absorption band spans from ca. 510 to 670 nm. ^{d} Measurements were performed in degassed CH$_2$Cl$_2$.

→ π* transition of the BIMe ligand. The absorption λ_{max} of the Soret band is relatively insensitive to the NHC ligand (*i.e.*, IMe, BIMe, IPr), and $\Delta\lambda_{max}$ is less than 4 nm in all cases for complexes with the same porphyrin scaffold. In addition, solvatochromism was found to be negligible for **2e** (Table S2 and Fig. S15†). The variation in λ_{max} of the Soret and Q bands in various solvents is less than 3 nm. These findings indicate predominantly porphyrin-based frontier molecular orbitals (FMOs) for Ir^{III}(por)–NHC complexes despite the nonplanarity of the porphyrin ring.

TD-DFT calculations on split Soret bands

To unveil the nature of the split Soret bands, time-dependent density functional theory (TD-DFT) calculations on the electronic transitions of **2a** were performed. The geometry of the ground-state singlet (S_0) was optimized, and vertically excited states were obtained *via* TD-DFT calculations. Notably, the composition and spin density distribution of the FMOs of **2a** are in excellent agreement with the classical four-orbital model proposed by Gouterman;[14] the contributions from the porphyrin ligand to HOMO−1, HOMO, LUMO and LUMO+1 amount to 99.8%, 95.5%, 97.5% and 97.7%, respectively (Fig. 7A). The simulated UV-vis absorption spectrum of **2a**, which shows high resemblance to the one obtained experimentally, is depicted in Fig. 7B. The calculations show that the Q bands at 565 nm originated mainly from HOMO → LUMO (S_1, 79%) and HOMO → LUMO+1 (S_2, 79%), which can be categorized as IL π → π* transitions of porphyrin. Nevertheless, assigning the nature of the transitions that constitute the low-energy (412 nm, S7/S8) and high-energy Soret bands (377 nm, S9/S10) is not straightforward, as both Soret bands consist of several vertical transitions involving 4 to 6 pairs of molecular orbitals. Accordingly, we examined the natural-transition orbitals (NTOs), which can provide a much more compact description of the excitations than the MOs. As listed in Table S3,† the excitation S7/S8, which relates to the low-energy Soret band, can be described as 68% porphyrin-based π–π* transition and 32% MLCT, while S9/S10, in association with the higher-energy Soret band, are attributed to MLCT transition mixed with intraligand charge transfer (ILCT) character.

Resonance Raman spectroscopy

Resonance Raman (RR) spectroscopy is an effective method to probe the nature of an electronic transition because the vibrations associated with the resonant chromophore can be selectively enhanced.[27] To help verify the parentage of the split Soret bands, the RR spectra of **2a** were recorded using excitation at 368.9 and 435.7 nm in MeCN. The former excitation wavelength is within the higher-energy Soret band, while the latter excitation wavelength is covered by the lower-energy Soret band. The experimental RR spectra and simulated ground-state Raman spectrum of **2a** from 1100–1800 cm^{-1} are shown in Fig. 8, and the assignment of vibrational bands is listed in Table S4.† The calculated Raman frequencies match well with the experimental ones. The RR spectra exhibit different intensity enhancements in response to excitation at 435.7 and 368.9 nm. The band at 1607 cm^{-1}, which results from C–C bond stretching within the tolyl rings and rocking of their hydrogen atoms without any contribution from the pyrrole rings, appears only under excitation at 435.7 nm. The other two enhancements at 1240 and 1206 cm^{-1} also result largely from the vibrational modes of the tolyl rings. The resonance in the excited state associated with the low-energy Soret band (435.7 nm) enhances the vibrational modes associated with tolyl rings more than those associated with pyrrole rings. In the case of excitation at 368.9 nm, four vibrational bands are relatively enhanced, namely, those at 1172, 1281, 1437 and 1521 cm^{-1}. Vibrational mode analysis shows that these four Raman bands all contain major components of the vibrational modes within the pyrrole rings. For example, the Raman band at 1437 cm^{-1} is mainly from symmetric stretching of the C_α–C_{meso}–C_α bonds and bending deformation of pyrrole rings, including rocking of the hydrogen atoms within the pyrrole rings. Thus, the resonance in the excited state associated with the higher-energy Soret band enhances the vibrational modes in pyrrole rings more than those in tolyl rings. The Raman bands that appear at 1356 and 1473 cm^{-1} under both excitation wavelengths (435.7 nm and 368.9 nm) are attributed to vibrational modes from both tolyl rings and pyrrole rings.
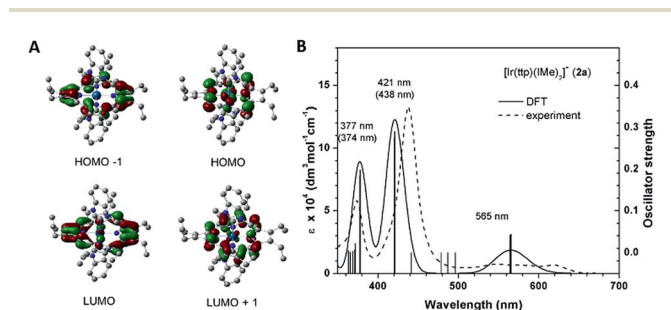

Fig. 7 (A) Frontier molecular orbitals (HOMO−1, HOMO, LUMO and LUMO+1), (B) simulated (solid line) and experimental (dashed line) UV-vis absorption spectra of **2a** (number in parenthesis is the experimental abs λ_{max}).
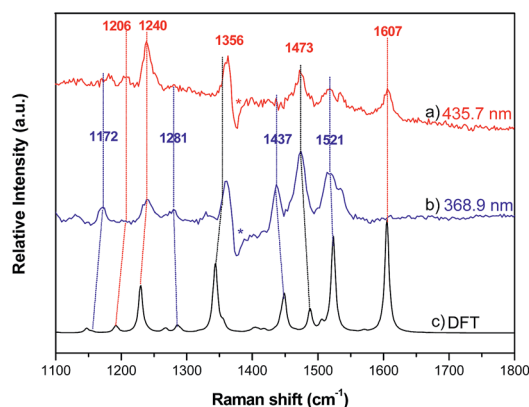

Fig. 8 Resonance Raman spectra of **2a** with excitation wavelengths of (a) 435.7 nm and (b) 368.9 nm; (c) Raman spectrum of **2a** calculated by DFT.

Nanosecond time-resolved absorption spectroscopy

The nanosecond time-resolved absorption difference (ns-TA) spectrum of **2c**, as a representative of bis-NHC complexes, is examined, and the following spectral features are noted (Fig. 9, top): (1) there are two intense positive absorption peaks at 388 and 468 nm, respectively, which are redshifted from the ground-state double Soret bands; (2) a broad, moderately intense positive absorption lies from *ca.* 550 nm to 800 nm. Indeed, despite a marked redshift of the excited-state Soret band by over 30 nm and a shorter-lived triplet state decay ($\tau_{468nm} = 2.6$ μs), the ns-TA spectrum of **2c** resembles the spectral profile of its counterparts **3**, **4**, and [Ir^{III}(oep)Cl(CO)] (Fig. 9, bottom).

Emission spectroscopy

Upon photoexcitation, complexes **1** and **2** (except **2a** and **2b**) produce NIR emission with λ_{max} spanning from 701 to 775 nm in degassed CHCl$_3$ solution (degassed CH$_2$Cl$_2$ for **2f**) at room temperature. The emission is assigned to the $^3(\pi, \pi^*)$ state of porphyrin; the emission spectra generally feature a broad though indistinct vibronic shoulder, akin to that of typical phosphorescent metalloporphyrins.[16,28] Several characteristics can be noted for the emissions of complexes **1** and **2**. (1) Their emission bands are much broader and are redshifted with respect to those of their counterparts. For instance, the Full-Width-at-Half-Maximum (FWHM) for **2c** is two to three times greater than those of [Ir^{III}(oep)Cl(CO)], **3** and **4** (*i.e.*, 66 nm *vs.* 26, 19 and 20 nm, respectively). In addition, the emission λ_{max} of **2c** is 701 nm, which is redshifted by more than 35 nm compared to those of its counterparts (Fig. 10). (2) The solution emission quantum yields and lifetimes at room temperature are substantially lower and shorter, respectively. For example, the Φ_{em} values of **2c**–**2e** supported by an oep ligand are only 0.03–0.66%, and τ ranges from 1.9 to 3.6 μs. This result is in stark contrast to the observations of [Ir^{III}(oep)Cl(CO)] and of the bis-ligand counterparts **3** and **4**, all of which show long-lived (τ = 55.2–124.7 μs) and strongly emissive $^3(\pi, \pi^*)$ states of porphyrin (Φ_{em} = 5.03–12.30%). Likewise, these observations hold for complexes supported by F$_{20}$tpp ligands **1d** and **2f** *versus* their

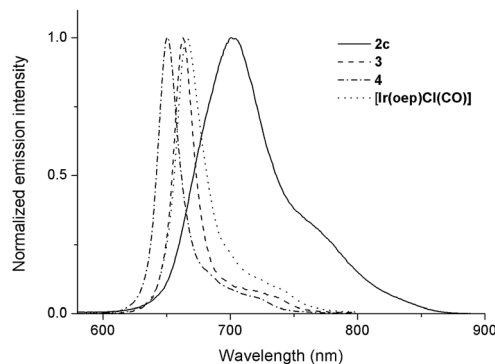**Fig. 10** Normalized emission spectra of **2c**, **3**, **4** and [Ir^{III}(oep)Cl(CO)] in degassed CHCl$_3$.

parent (Φ_{em} = 0.08–0.29% *vs.* 2.92%; τ = 0.5–1.7 *vs.* 101.0 μs). (3) Modification of NHC ligand exerts a negligible effect on both the emission profile and emission λ_{max}, as demonstrated for **2c**–**2e** (Fig. S16†). (4) Increasing the number of NHC ligands, as shown in the case of [Ir^{III}(F$_{20}$tpp)Cl(CO)], **1d** and **2f**, results in a progressive redshift in the emission λ_{max} from 676 to 754 nm (Fig. S17†). (5) Varying the porphyrin ligand causes the emission λ_{max} to range from 701 to 775 nm, and λ_{max} was found to increase in the order oep < F$_{20}$tpp < ttp ≈ tmp. Similar findings have previously been reported for Pd^{II}- and Pt^{II}-porphyrin complexes.[28]

Photochemistry

Recently, a panel of Ir^{III}–porphyrin[16d] and Ir^{III}–corrole[29] complexes were found to be efficient singlet oxygen photosensitizers (Table 5).

In particular, the quantum yield of singlet oxygen production (Φ_{so}) by BODIPY conjugates of Ir^{III}-ttp upon excitation at 690 nm is up to 0.85. In this work, [Ir^{III}(por)(NHC)$_2$]$^+$ complexes were also found to be highly efficient photosensitizers for singlet oxygen production. With reference to the ^{1}O$_2$ emission intensity (λ_{max} = 1270 nm) of H$_2$tpp (Φ_{so} = 0.55 in CHCl$_3$),[30] the Φ_{so} values of oxygen-saturated CHCl$_3$ solutions of **2a** and **2c** were found to be 0.64 and 0.88, respectively, upon excitation at their Soret bands (Fig. 11). As described in the previous section, upon bis-ligation of the NHC ligand to iridium porphyrin, complexes **2** show redshifted and broadened Soret and Q bands, resulting in broad coverage of the visible light spectral region. This
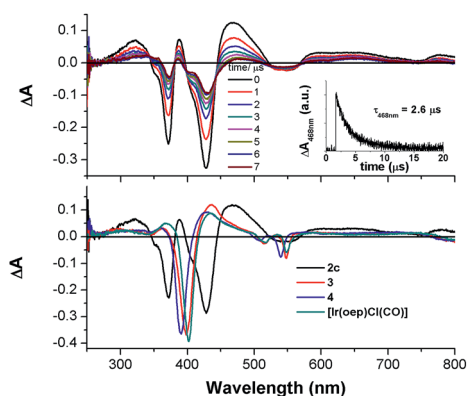
Fig. 9 (Top) The ns-TA spectra of **2c** evolved from 0 to 7 μs; inset: Decay kinetics of absorption difference at 468 nm. (Bottom) Overlaid ns-TA spectra of **2c**, **3**, **4**, and [Ir(oep)Cl(CO)] recorded at 0 μs.

Table 5 The quantum yield of singlet oxygen production (Φ_{so}) by **2a**, **2c** and reported Ir^{III}–porphyrin and corrole complexes

Complex	Φ_{so}
2a	0.64[a]
2c	0.88[a]
[Ir^{III}(corrole)(pyridine)$_2$]	0.09–0.15[a29]
[Ir^{III}(ttp)(aza-BODIPY)]	0.79–0.85[b16d]

[a] Measured in CHCl$_3$ with reference to the ^{1}O$_2$ emission intensity of H$_2$tpp. [b] Measured in CH$_2$Cl$_2$ with reference to the photooxidation of 1,3-diphenylisobenzofuran by methylene blue.
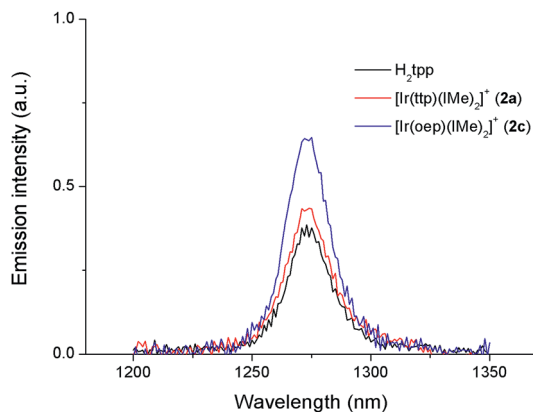
Fig. 11 Singlet oxygen emission spectra of H$_2$tpp, **2a** and **2c** in O$_2$-saturated CHCl$_3$.

spectral feature and the high singlet oxygen quantum yield enable **2** to act as a photosensitizer for catalytic aerobic oxidation reactions and prompted us to examine the aerobic oxidation of secondary amines and arylboronic acids. When a solution of dibenzylamine treated with 0.1 mol% of **2a** was bubbled with O$_2$ under light irradiation ($\lambda > 400$ nm) at room temperature for 5 h, the corresponding imine was produced in 92% yield with complete substrate conversion (entry 1, Table 6). Changing the photosensitizer to **2c** led to a higher product yield of 99% (entry 2, Table 6). The reaction also worked for substrates with halogen/methyl substituted benzyl groups and *tert*-butyl groups, furnishing the respective imine products in 96–99% yields (entry 3–5, Table 6). In another reaction, irradiating ($\lambda > 400$ nm) solutions of *para*-substituted arylboronic acids in the presence of diisopropylamine and 0.5 mol% of **2c** for 3 h at room temperature gave rise to the corresponding aryl alcohols in yields of 82 to 99% (Table 7). The control experiments indicated the necessity of **2a** or **2c** for both reactions (entry 6, Table 6; entry 6, Table 7). The mechanisms of the photochemical reactions were investigated by experiments on

Table 6 Light-induced aerobic oxidation of secondary amine to imine, catalyzed by **2a** or **2c**[a]


Entry	PS	X/R	Convn.[b] (%)	Yield[c] (%)
1	**2a**	H/Bn	100	92
2	**2c**	H/Bn	100	99
3	**2c**	Cl/^{t}Bu	100	99
4	**2c**	Br/^{t}Bu	100	99
5	**2c**	Me/^{t}Bu	100	96
6	—	H/Bn	<5	n.d.[d]

[a] Reaction conditions: dibenzylamine (0.1 mmol) and catalyst (0.1 μmol) in MeCN (1.5 mL), O$_2$ bubbling, xenon lamp (>400 nm). [b] Determined by ^{1}H NMR analysis of the crude reaction mixture. [c] Determined by ^{1}H NMR analysis using 1,1-diphenylethylene as an internal standard. [d] n.d. = not determined.

Table 7 Light-induced aerobic oxidation of arylboronic acid catalyzed by **2c**[a]

Entry	R	Convn. (%)[c]	Yield (%)[d]
1	Cl	100	92%
2	Br	100	98%
3	CHO	100	98%
4	Ph	100	82%
5	CN	100	99%
6[b]	Br	<5%	n.d.[e]

[a] Reaction conditions: arylboronic acid (0.1 mmol), diisopropylamine (0.4 mmol) and **2c** (0.5 μmol) in DMF (1.5 mL), O$_2$ bubbling, xenon lamp (>400 nm). [b] No **2c** added. [c] Determined by ^{1}H NMR analysis of the crude reaction mixture. [d] Determined by ^{1}H NMR analysis using 1,1-diphenylethylene as an internal standard. [e] n.d. = not determined.

the quenching of **2a** or **2c**. The presence of a large excess (1000 equiv.) of amine (*i.e.*, dibenzylamine and diisopropylamine) or arylboronicacid (*i.e.*, 4-chlorophenylboronic acid) did not have significant effect on the lifetimes of the photogenerated **2a*** and **2c*** under degassed conditions (Fig. S19†). Nevertheless, the lifetimes of **2a*** and **2c*** were considerably reduced to 0.16 μs and 0.09 μs in oxygen-saturated solution, respectively (Fig. 12). On the basis of these findings, both photoinduced aerobic amine oxidation and arylboronic acid oxidation reactions begin with the oxygen quenching of photogenerated **2a***/**2c*** by energy transfer to give ^{1}O$_2$, which subsequently oxidizes the secondary amines to imines or the arylboronic acids to aryl alcohols.

Anticancer properties

We have previously reported various cationic metalloporphyrins, particularly gold(III) porphyrins, and metal–NHC complexes that
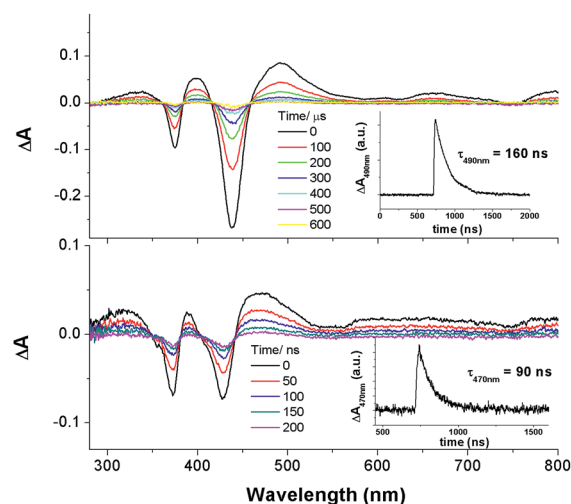

Fig. 12 Nanosecond time-resolved absorption difference spectra of **2a** in O$_2$-saturated MeCN (top) and **2c** in O$_2$-saturated DMF (bottom). Inset: decay kinetic of absorption difference at 490 nm (top) and 470 nm (bottom).

exhibit promising anticancer and antitumor activities.[31] In this work, iridium(III) porphyrin complexes bearing NHC ligand(s) were found to be stable against ligand exchange with DMSO or glutathione up to an 24 h incubation, as determined by UPLC-QTOF mass spectrometry (Fig. S21 and S22†). DMSO-substituted forms (ca. 8%) were found for **3** (Fig. S21f†). All of the cationic iridium(III) complexes exhibit potent cytotoxicity towards a panel of human cancer cell lines with submicromolar IC_{50} values, while **3** shows generally reduced cytotoxicity (Table 8). Among the bis-NHC complexes, the higher cellular uptake of **2c** (with octaethylporphyrin) than that of **2a** (with meso-tetratolylporphyrin) and **2f** (with meso-tetrakis(pentafluorophenyl)porphyrin) results in higher cytotoxicity towards different cancer cell lines. In addition, the charge-neutral [Ir^{III}(oep)Cl(CO)], which showed the lowest cellular uptake and lipophilicity, is relatively noncytotoxic, with an IC_{50} value >50 μM to all the cancer cell lines. These findings highlight that the cationic character and porphyrin scaffold of iridium(III) bis-NHC complexes are crucial for facilitating efficient accumulation in cells for anticancer activities. On the basis of the potent in vitro cytotoxicity of **2c**, its in vivo antitumor properties were examined. Nude mice bearing NCI-H460 human non-small cell lung cancer xenografts were administered **2c** (3 mg kg^{-1}) via intravenous injection thrice weekly. The tumor size was reduced by 41% after a 16 day treatment without apparent toxicity, including body weight loss and death (Fig. 13). In view of the advantageous photophysical properties (including high emission quantum yield and long-lived electronic excited state) of **2c** among the bis-NHC iridium(III) complexes, cellular imaging of **2c** was performed to examine its subcellular localization in NCI-H460 cells. As shown in Fig. 14A, the resulting images clearly revealed that the red-emitting **2c** mainly colocalized with the green-emitting stain of the endoplasmic reticulum (ER-Tracker) with a high Pearson's correlation coefficient (R) of 0.903. In contrast, a relatively poor overlap was observed between the fluorescence images of the complex and Mito-Tracker green or Lyso-Tracker green, with an R-value of 0.548 and 0.210. These findings indicated that **2c** accumulated mainly
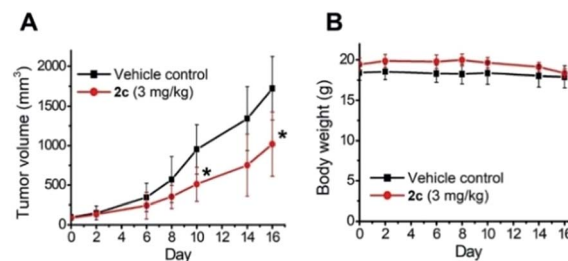

Fig. 13 In vivo antitumor activity of complex **2c** in nude mouse model bearing NCI-H460 xenograft. (A) Tumor volume and (B) body weight of mice. Data are expressed as the mean ± standard error; *p < 0.05.

in the ER and only somewhat in the mitochondria or lysosome in NCI-H460 cells. We therefore examined if **2c** induced ER stress to the NCI-H460 cells.[32] By the western blot analysis, the ER stress-associated proteins including CHOP and phosphorylated eIF2α were found to be dose- and time-dependently upregulated upon treatment with **2c** compared to the DMSO vehicle (Fig. 14B), confirming the induction of ER stress. The impact of **2c** on mitochondria was also examined by monitoring the changes in mitochondrial membrane potential (MMP, $\Delta\Psi_m$). With the use of a MMP-dependent ratiometric fluorescence probe (JC-1), time-dependent decrease in MMP of NCI-H460 cells was shown upon the treatment of **2c**, as indicated by the progressive change in fluorescence from red to green compared with DMSO vehicle (Fig. 14C).

Photocytotoxicity

Prompted by the finding that the iridium(III) porphyrin complexes are excellent singlet oxygen photosensitizers, we examined their photocytotoxicity. NCI-H460 lung cancer cells incubated with the complexes were exposed to a low dose of visible light irradiation (2.8 mW cm^{-2}) for 1 h. The cytotoxicity of the iridium(III) porphyrin complexes increased markedly by 10- to 27-fold upon irradiation, and [Ir^{III}(oep)(I^{i}Pr)$_2$]$^+$ (**2e**)

Table 8   In vitro cytotoxicity of the selected iridium(III) porphyrin complexes against a panel of human cancer cell lines[abc]

| | IC_{50} (μM)[b] | | | | | IC_{50} (μM) | | | | |
	HeLa	HepG2	MCF-7	HCT116	HCC827	NCI-H460 (dark)	NCI-H460 (light)	PI[c]	Uptake[d]	Log P[e]
1d[f]	0.37 ± 0.10	1.60 ± 0.21	0.71 ± 0.04	0.42 ± 0.06	0.55 ± 0.11	0.46 ± 0.10	0.04 ± 0.003	11.5	235.9 ± 9.81	2.67
2a	0.17 ± 0.1	2.1 ± 0.3	0.65 ± 0.2	0.14 ± 0.04	2.29 ± 0.50	1.22 ± 0.03	0.11 ± 0.08	11.1	147.6 ± 6.4	3.03
2c	0.03 ± 0.01	0.93 ± 0.1	0.16 ± 0.1	0.14 ± 0.1	1.1 ± 0.3	0.15 ± 0.05	0.009 ± 0.004	16.7	309.7 ± 46.7	2.96
2e	0.10 ± 0.1	2.4 ± 0.2	0.73 ± 0.5	0.11 ± 0.03.	0.69 ± 0.01.	0.16 ± 0.04	0.006 ± 0.002	26.7	158.7 ± 29.5	3.23
2f	0.10 ± 0.1	0.94 ± 0.1	0.26 ± 0.1	0.4 ± 0.2	1.23 ± 0.10	0.31 ± 0.04	0.03 ± 0.002	10.3	131.3 ± 10.2	2.76
3	7.9 ± 0.5	>100	>100	23 ± 3.3	50 ± 3.6	2.9 ± 0.02	0.12 ± 0.02	24.2	116.2 ± 20.6	3.11
4	0.10 ± 0.01	1.32 ± 0.10	0.12 ± 0.02	0.25 ± 0.08	1.27 ± 0.32	0.11 ± 0.005	0.005 ± 0.001	23.1	305.1 ± 57.2	2.83
[Ir^{III}(oep)Cl(CO)]	>50	>50	>50	>50	>50	>50	19.70 ± 1.0	>2.5	34.1 ± 2.8	2.38
Cisplatin	3.80 ± 0.51	6.18 ± 0.82	13.20 ± 1.03	6.94 ± 0.54	9.61 ± 0.81	3.96 ± 0.48	4.61 ± 0.31	0.86	—	—

[a] HeLa, cervical epithelial carcinoma; HepG2, hepatocellular carcinoma; MCF-7, breast carcinoma; HCT-116, colorectal carcinoma; HCC827, non-small cell lung carcinoma; NCI-H460, non-small cell lung carcinoma. [b] IC_{50} values were examined by MTT assay after incubation of drugs for 72 h. [c] PI = IC_{50}(dark)/IC_{50}(light). [d] Cellular uptake was determined by the iridium content (μg) in the cellular proteins (g) after treatment of the NCI-H460 cells with each complex (1 μM) for 2 h. [e] Lipophilicity was determined by measuring the ratio of the amount of iridium (μg) in each complex partitioned in n-octanol and saline solution (0.9%, w/v).
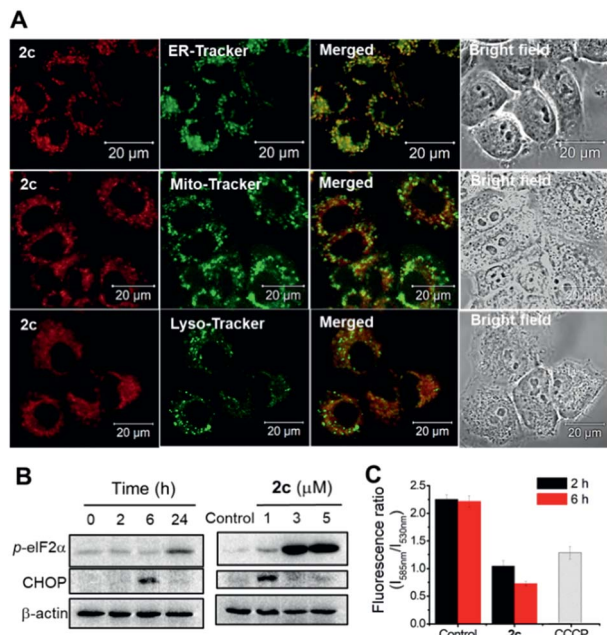
Fig. 14 (A) Confocal microscopy imaging of NCI-H460 cells treated with complex 2c (1 μM; $\lambda_{ex} = 555$ nm, $\lambda_{em} = 650$–750 nm) for 2 h and organelle trackers, including ER-Tracker green, Mito-Tracker green and Lyso-Tracker green (50 nM, $\lambda_{ex} = 488$ nm, $\lambda_{em} = 500$–530 nm) for 15 min. The merged images of red and green channels, and the bright field were also shown. Scale bar: 20 μm. (B) Western blot analysis of ER stress protein markers in NCI-H460 cells after treatment with 2c in time- and dose-dependent manner. (C) Effect of 2c (1 μM) on mitochondrial membrane potential (MMP) analyzed by the fluorescence ratio of NCI-H460 cells stained with JC-1 ($\lambda_{ex} = 488$ nm, $\lambda_{em} = 530$ nm (green) and 585 nm (red)). Treatments with carbonylcyanide m-chlorophenylhydrazone (CCCP, 50 μM, 10 min) and DMSO were served as positive and vehicle controls, respectively.
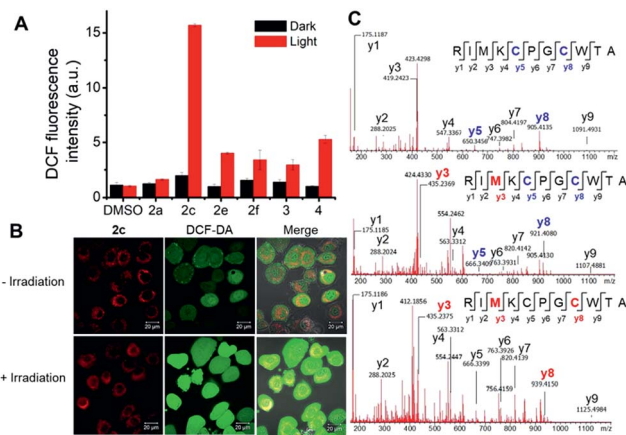

Fig. 15 (A) Generation of ROS examined by DCF fluorescence measurement in NCI-H460 cells treated with or without iridium(III) porphyrin complexes (1 μM) for 2 h with or without irradiation by visible light. (B) Confocal microscopy imaging of ROS generation in cells incubated with complex 2c with or without irradiation by visible light. Scale bar: 20 μm. (C) Photooxidation of peptide from thioredoxin by 2c. ESI-MS/MS spectra of the triply charged disulfide-bridged peptide (m/z 421.8638; top) and oxidized peptides (m/z 427.1954; middle, m/z 433.1978; bottom). Fragments with blue labels indicate sites of disulfide bond formation, and red labels represent oxidative modification sites.

showed the largest enhancement among the complexes examined (Table 8 and Fig. S23†). [Ir^{III}(oep)(IMe)$_2$]$^+$ (2c), [Ir^{III}(oep)(I^{i}Pr)$_2$]$^+$ (2e) and [Ir^{III}(oep)(py)$_2$]$^+$ (4) exhibited very potent cytotoxicity with nanomolar IC$_{50}$ values. For the mono-NHC complex [Ir^{III}(F$_{20}$tpp)(BIMe)(NH$_3$)]$^+$ (1d′), significant potentiation of the cytotoxicity was also found under the same conditions. The cytotoxicity of [Ir^{III}(oep)Cl(CO)] was also evaluated for comparison. This complex is relatively noncytotoxic in the dark with an IC$_{50}$ value >50 μM and increased to 19.7 ± 1.0 μM upon visible light irradiation. For cisplatin, the difference in the phototoxicity index (PI) was <1, indicating an absence of photoinduced cytotoxicity under our experimental conditions. Thus, the cytotoxicity of the iridium(III) porphyrin complexes with the incorporation of axial bis-carbene ligands is significantly enhanced under light irradiation.

To examine the relationship between photocytotoxicity and the photosensitizing properties of the complexes, we measured the cellular reactive oxygen species (ROS) generation using the ROS probe H$_2$DCF-DA after treatment of cancer cells with the iridium(III) porphyrin complexes. As shown in Fig. 15A, no significant change in DCF fluorescence was observed in NCI-H460 lung cancer cells incubated with the complexes in the dark. Exposure to visible light irradiation resulted in increased

DCF fluorescence intensity, revealing elevated cellular ROS levels. In particular, a 10-fold elevation in ROS levels in cells treated with 2c was observed. The result was further corroborated by the strong green fluorescence observed from DCF when cells were treated with 2c followed by light irradiation (Fig. 15B). These results confirmed the generation of ROS, possibly $^1O_2$, in NCI-H460 cells treated with Ir(III) complexes upon visible light irradiation. We further examined the possibility of protein oxidation as a consequence of photoinduced oxidative stress caused by 2c. A peptide (RIMKCPGCWTA) from thioredoxin (Trx) was employed as a model to investigate the possible oxidative modification sites by electrospray ionization tandem mass spectrometry (ESI-MS/MS). The peptide was found to undergo oxidative modifications in the presence of 2c upon irradiation. Three different types of oxidized products, including the formation of a disulfide bridge and the oxidation of the sulfur atoms of cysteine and methionine, were characterized (Fig. 15C, S25 and Tables S6–S8†). The peptide alone as a control was shown to remain unchanged when incubated in the dark or upon light irradiation (Fig. S24 and Table S5†). As shown in Fig. 15C and S25,† three triplycharged species were detected with mass differences of −0.671 (top), +4.660 (middle) and +10.662 (bottom) Da, respectively, from the unmodified peptide. Further MS/MS analysis revealed that the most intense peak (m/z 421.8638; Fig. 15C (top), Table S6†) corresponds to the formation of an intramolecular disulfide bond, in which the resulting fragment y5 and y8 ions bearing free cysteine and cysteine thioaldehyde residues, respectively, were observed when comparing with the peptide alone (Fig. S26†).

Moreover, additional oxidative modification of the methionine residue to give sulfoxide (y3) with a shift of +16 Da was also found on the disulfide-bridged peptide (m/z 427.1954; Fig. 15c

(middle), Table S7†). In addition, another oxidation product (*m/z* 433.1978) with a mass increment of +10.662 in a triply charged state is ascribed to the addition of two oxygen atoms (+32 Da) in the singly charged species. MS/MS sequence analysis displayed the identified y-ions, which are attributed to the oxidized methionine (y3; O-Met, Met +16 Da) and cysteine (y8; O-Cys, Cys +16 Da) of the peptide (Fig. 15c (bottom) and Table S8†). These results show that treatment with **2c** combined with light activation promoted the oxidation of cysteine and methionine residues through a singlet oxygen-mediated mechanism.

To examine the photoinduced cytotoxicity, the apoptotic cell death and cell cycle progression of the cancer cells treated with **2c** and visible light irradiation were analyzed by flow cytometry. NCI-H460 cells were incubated with **2c** at 0.1 μM, a concentration that could not lead to strong antiproliferative effects in the dark. Upon exposure to light irradiation, the proportion of cells treated with **2c** undergoing apoptotic cell death increased from 5.9% to 81.7%, as shown by the annexin-V-FITC/propidium iodide assay (Fig. 16A). On the other hand, complex **2c** (0.1 μM) did not exhibit a marked effect on the progression of the cell cycle in the dark, showing only a mild increase in the G_0/G_1-population from 59.6% to 66.3%. In agreement with the annexin-V/propidium iodide flow cytometry results above, visible light irradiation led to a significant increase in the sub-G_1 population (from 2.2% to 96.9%) as a result of extensive DNA fragmentation due to cell death (Fig. 16B). We also examined the antiangiogenic property of **2c** in the inhibition of endothelial cell tube formation. As shown in Fig. 16C, moderate inhibition of MS-1 cell tube formation was observed after treatment of the complex in the dark, while tube formation was completely abrogated upon light irradiation. The above results showed that a low dose of **2c** causes very low-level cellular damage in the dark but could induce pronounced apoptosis and inhibition of angiogenesis upon visible light irradiation. Noticeably, other iridium porphyrin complexes were also observed to exert similar effects (Fig. S27–S29†). The *in vivo* photoinduced therapeutic

efficacy of **2c** was also examined. NCI-H460 tumor-bearing mice were divided into four groups, vehicle control, **2c** (3.0 mg kg^{-1}), vehicle control with irradiation, and **2c** (3.0 mg kg^{-1}) with irradiation, and subjected to two intratumoral injections of the compounds in a period of 15 days. Mice in the irradiation groups were injected with **2c** or solvent vehicle followed by exposure of the tumor site to white light (400–800 nm) at a power density of 110 mW cm^{-2} for 30 min on the first and seventh days. The other two groups of mice received the same treatment without irradiation as a control. As shown in Fig. 17A, the tumor growth of mice treated with **2c** and irradiation was markedly decreased by 72% in comparison to that of the vehicle
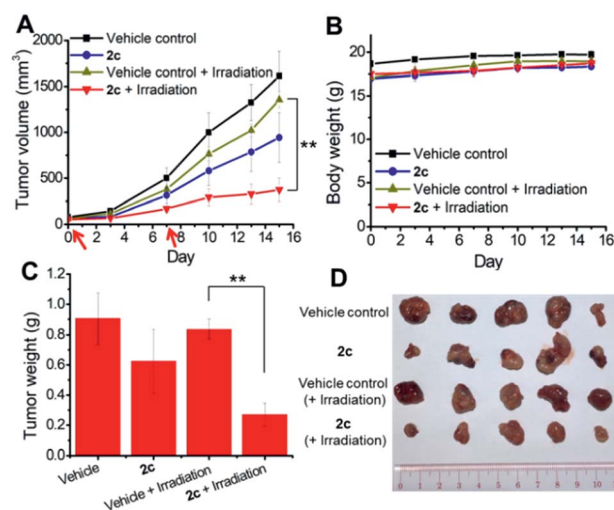
Fig. 17 *In vivo* antitumor effects of complex **2c** in nude mouse model bearing NCI-H460 lung cancer xenografts. (A) Tumor volume. (B) Body weight of mice. (C) Tumor weight after the experiment. Red arrows indicate the injection of the mice with **2c** together with irradiation on day 0 and day 7. (D) Photo of tumors of each group after treatment for 15 days. Data are expressed as the mean ± standard error; **p < 0.01.
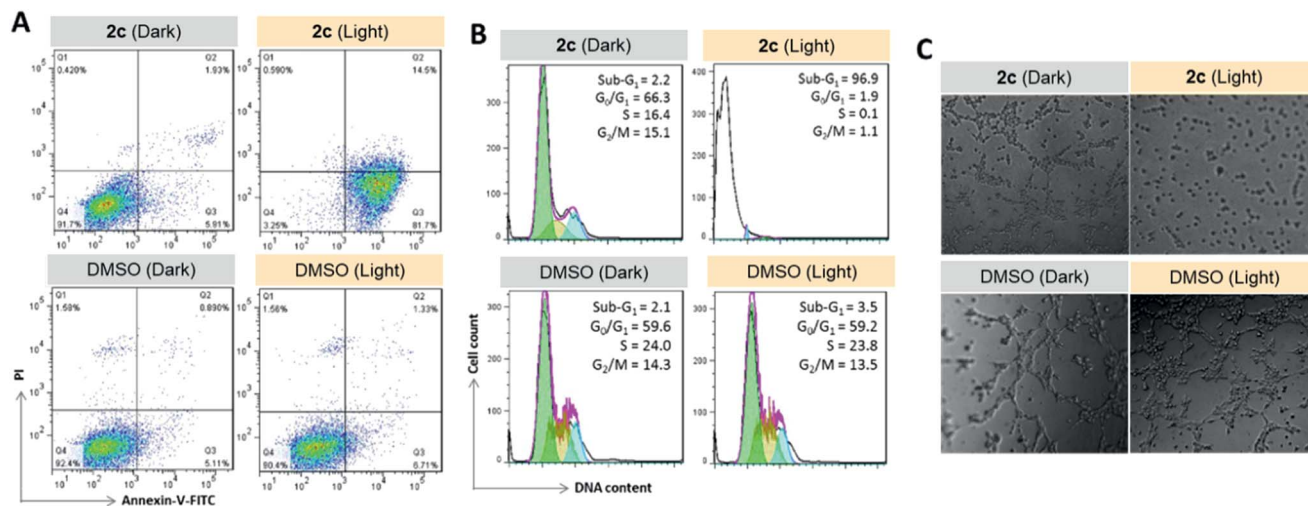
Fig. 16 Anticancer properties of **2c** (0.1 μM) upon visible light irradiation. (A) Apoptosis/necrosis in NCI-H460 cells as examined by flow cytometry of annexin-V-FITC/propidium iodide-stained cells. (B) Cell cycle progression in NCI-H460 cells as examined by flow cytometry. (C) Inhibition of angiogenesis of MS-1 endothelial cells.

group with light irradiation after only two injections. In contrast, treatment with **2c** without irradiation was able to inhibit tumor growth by only 41%. All of the mice displayed negligible changes in body weight throughout the treatment period (Fig. 17B). Moreover, the tumor weight of **2c**-treated mice in the photoirradiation group was found to be much lower than that in the dark control group (Fig. 17C and D), demonstrating the markedly enhanced antitumor efficacy of the combination of dark and photoinduced tumor inhibitory activities.

Discussion

The coordination of the NHC ligand to Ir^{III}–porphyrins causes several major alterations to the spectral and photophysical parameters compared to those of the $[Ir^{III}(por)Cl(CO)]$ and $[Ir(por)L_2]^+$ (L = isocyanide, pyridine or imidazole) complexes.[16a]

Split Soret band

All NHC complexes in this work feature two distinct Soret bands with comparable intensity. Metalloporphyrins showing split Soret bands are classically termed hyperporphyrins.[14,15c] The valence of the metal ions and the nature of the axial ligand(s) are known to dictate this spectral attribute. Hyperporphyrins can be divided into p-type and d-type. In d-type hyperporphyrins, which are relevant to our case, the metal ions are generally trivalent or at a higher oxidation state with low metal reduction potential and partially filled $d\pi$ orbitals. As a result, the extra Soret band is attributed to the ring-to-metal LMCT transition of $a_{1u}(\pi), a_{2u}(\pi) \rightarrow e_g(d\pi)$ character. Metalloporphyrins of Fe^{III}, Mn^{III} and Cr^{III} ions are canonical examples of this type.[14] However, this scenario is not applicable to **1** and **2**, which contain a d^6 Ir^{III} ion, because all nominal $d\pi$ (d_{xz}, d_{yz}) orbitals are fully occupied, and no such LMCT transition can take place in the UV-visible spectral region. Notably, the double Soret band found in d^6 metalloporphyrin is not unique to our Ir–NHC system; a few Ir^{III}- and Rh^{III}-porphyrin complexes bearing phenyl(alkoxycarbonyl)carbene or NHC with a *trans* methyl ligand, recently described by Woo and co-workers, also exhibit this spectral attribute.[6,33] Woo and co-workers suggested that orbital mixing with relatively low-energy doubly excited states, $[e_g(d\pi)]^3[a_{1u}(\pi), a_{2u}(\pi)]^3[e_g(\pi^*)]^2$, may be responsible for the extra Soret band. Our TD-DFT calculations on **2a** indicated that the high-energy (extra) Soret band mainly comes from electronic transitions from the hybrid of the iridium d_{xy} orbital and the π orbitals of the porphyrin's peripheral tolyl groups to the core π^* porphyrin orbitals (pyrrole rings + mesocarbons), which is best described as an MLCT transition with mixed ILCT character, while the low-energy (conventional) Soret band mainly comes from $\pi \rightarrow \pi^*$ IL transitions within the porphyrin ligand. Based on RR experiments, the independent excitation of **2a** at the extra Soret band (435.7 nm) and at the conventional Soret band (368.9 nm) results in the selective enhancement of different vibrational modes, corroborating that the excited states associated with the two bands have different characteristics. In particular, the former (MLCT) excitation primarily

enhances vibrational modes involving the core skeleton to which the Ir(III) ion is directly linked, while the latter (π–π^*) excitation enhances mainly the vibrational modes within the tolyl rings to which the porphyrin core is connected. Overall, the experimental findings from the RR study of **2a** concur with the conclusion from DFT calculations that the extra Soret band is associated with an Ir-to-porphyrin MLCT excitation.

Interestingly, the intensity of the MLCT band is found to vary with the number of NHC ligands, as exemplified in the series $[Ir^{III}(F_{20}tpp)Cl(CO)]$ (log $\varepsilon_{MLCT} = 0$), $[Ir^{III}(F_{20}tpp)(IMe)Cl]$ (**1c**) (log $\varepsilon_{MLCT} = 4.62$) and $[Ir^{III}(F_{20}tpp)(IMe)_2]^+$ (**2f**) (log $\varepsilon_{MLCT} = 4.89$). Thus, NHC ligands play an indispensable role in enhancing the allowedness of the MLCT transition. Notably, the extra Soret band (LMCT band) of high-spin $[Mn^{III}(tpp)]^+$ complexes, typical d-type hyperporphyrins, also displays comparable intensity to their 'conventional' π–π^* Soret band.[14,34] This observation was explained by the fact that the high-lying $d\pi(d_{xz}, d_{yz})$ orbitals of the Mn^{III} ion can undergo substantial interaction with the porphyrin $e_g(\pi^*)$ orbitals due to their energetic proximity, which leads to strong mixing of the $\pi(por) \rightarrow d\pi(Mn^{III})$ LMCT and Soret π–π^* states.[14,33] Thus, we propose that in our case, the strongly electron-donating NHC ligand(s) can boost the Ir $d\pi$ orbitals to a higher level at which they can mix efficiently with the porphyrin π^* orbitals. This phenomenon in turn enables borrowing of the oscillator strength from the Soret π–π^* transition to enhance the allowedness of the MLCT transition. In fact, the intensity of the MLCT Soret band increases at the expense of the π–π^* Soret band from $[Ir^{III}(F_{20}tpp)Cl(CO)]$, **1c** to **2f** with log ε_{MLCT}/log ε_{Soret} values of 0/5.42, 4.62/5.10 and 4.89/5.00, respectively. Incidentally, the possibility that ruffling deformation also contributes to enhancing the MLCT band intensity cannot be ruled out, as all reported Ir^{III}- and Rh^{III}-porphyrin complexes with such an extra Soret band were found or calculated to have a ruffled porphyrin ring.[5b,6,33]

Spectral redshift, reduced emission quantum yield and lifetime

The ruffled porphyrin ring, as revealed by X-ray crystallographic analysis, is a key structural feature of $[M^{III}(por)\text{-}NHC]$ (M = Ir and Rh) complexes.[5b,6] Here, the extent of ruffling increases with the number of NHC ligands owing to the enhanced steric congestion. In the literature, out-of-plane ring deformation in the form of either ruffling or saddling is well documented to engender a spectral redshift in both free base porphyrins and metalloporphyrins; the extent of redshift is usually proportional to the magnitude of distortion, albeit in a nonlinear fashion.[8] In addition, metalloporphyrins with deformed porphyrin rings are known to undergo rapid macrocyclic inversion in both the ground state and the excited state. This inversion generally leads to diminished luminescence and emission lifetime compared to those of planar metalloporphyrins as a result of the surging nonradiative decay activities in the form of low-energy out-of-plane vibrations in the excited state.[8a,e,9c] Indeed, the mono- and bis-NHC complexes of Ir(III)-porphyrin in this work exhibit the aforementioned photophysical attributes of

nonplanar metalloporphyrins; their Soret and Q bands and their porphyrin-based $^3(\pi, \pi^*)$ emissions are markedly redshifted by up to 80 nm with respect to the parental $[Ir^{III}(por)Cl(CO)]$ complexes and bis-ligand analogs (Table 4; Fig. 6 and 10). Furthermore, the emission quantum yield and lifetime drop to less than 0.7% and 3.6 μs respectively, with the bis-NHC analogs suffering more severely. As revealed by the excited-state photophysical parameters in Table 9, the increase in the non-radiative decay constant of the emissive excited state of up to 200 times underlies the decrease in emission quantum yield and lifetime, although the radiative decay rate constants increase slightly by 3–14-fold.

Photosensitized singlet oxygen generation

Metalloporphyrins and their derivatives, such as metallocorroles, are important classes of photochemical singlet oxygen sensitizers that exhibit good biocompatibility, strong visible light absorption, high triplet-state quantum yields and long triplet-state lifetimes.[29,35] They have been extensively studied as sensitizers for photodynamic therapy and photo-driven aerobic oxidation reactions.[28c,36,37] Several iridium(III)-porphyrin and corrole complexes have recently been found to exhibit such favorable inherent properties and are capable of generating singlet oxygen photochemically.[16d,29] In particular, two σ-bonded aza-BODIPY complexes of Ir^{III}(ttp) were reported to have Φ_{so} values of 0.79 and 0.85, which are more than 100 times greater than those of the respective free aza-BODIPY ligands, revealing the effectiveness of the iridium(III) porphyrin moiety in promoting singlet oxygen sensitization.

Two cationic bis-NHC complexes examined in this work, **2a** and **2c**, were found to be efficient photosensitizers for the photoinduced aerobic oxidation of secondary amines and arylboronic acids. Quenching experiments suggested that singlet oxygen generated by quenching of the excited state of **2a** or **2c** is presumably the active oxidant for these photooxidation reactions. This finding is in good agreement with their high Φ_{so} values of 0.64 and 0.88, respectively. The singlet oxygen quantum yield of a photosensitizer is determined by the triplet-excited-state quantum yield and the efficiency of energy transfer

from the triplet excited state to molecular oxygen.[35a] Considering that the heavy iridium ion with its large spin orbit coupling constant (ξ_{Ir} = 3909 cm^{-1}) often confers an ultrafast intersystem crossing rate and triplet-excited-state formation yield close to unity,[38] the higher singlet oxygen formation quantum yield of **2c** than of **2a** is attributed to the former having a longer triplet-state lifetime (τ = 2.3 vs. 0.4 μs) (Fig. S19†).

Stability, cytotoxicity and photochemical activities

Our previous works showed that porphyrin ligand can stabilize gold(III) ion against demetallation under physiological conditions rendering gold(III) porphyrins to display effective anticancer activity against multiple cancer cell types in vitro and in vivo.[31a–d] We have also found that as a result of strong σ-donating property of NHC ligand, pincer gold(III) and platinum(II) complexes containing NHC auxiliary ligand are stable against ligand exchange reaction under physiological conditions and these complexes display potent antitumor properties.[31e,39] By using both porphyrin and NHC ligands altogether, we prepared a panel of stable octahedral iridium(III) porphyrin complexes containing NHC ligand that exhibit potent in vitro anticancer activities and show significant inhibition of tumor growth in vivo upon photo-irradiation.

The Ir(III) porphyrin complexes bearing bis-NHC or mono-NHC axial ligand(s) display a good stability against ligand exchange with DMSO solvent or glutathione (Fig. S21 and S22†). Complex **3** bearing bis-isocyanide ligands is more substitution labile (Fig. S21f†). Most of the $[Ir^{III}(por)(NHC)_2]^+$ complexes exhibit cytotoxicity to different cancer cell lines with IC_{50} values down to submicromolar concentrations (Table 8). Incorporation of NHC ligand(s) into iridium porphyrin increases lipophilicity of the complexes hence their cellular uptake and accumulation in cancer cells. Complex **2f** with meso-tetrakis (pentafluorophenyl)porphyrin ligand displays the lowest cellular uptake and lipophilicity among the bis-NHC complexes. Cationic iridium porphyrin complexes show more efficient cellular internalization and hence increase in anticancer activity as indicated by lower IC_{50} values compared to those of the neutral complex $[Ir^{III}(oep)Cl(CO)]$ and the isoelectronic

Table 9 k_r and k_{nr} values of Ir^{III}(por) complexes in CHCl$_3$ solutions at 298 K

Complex		Φ_{em} [$\times 10^{-2}$]	τ_{em}/μs	k_r^a [$\times 10$]/s	k_{nr}^b [$\times 10^3$]/s
$[Ir^{III}(tmp)Cl(CO)]$		0.22	77.2	2	13
$[Ir^{III}(oep)Cl(CO)]$		5.03	83.3	60	11
$[Ir^{III}(F_{20}tpp)Cl(CO)]$		2.92	101.0	29	10
$[Ir^{III}(tmp)(IMe)Cl]$	**1a**	0.05	1.8	28	555
$[Ir^{III}(tmp)(BIMe)Cl]$	**1b**	0.06	2.3	26	435
$[Ir^{III}(F_{20}tpp)(BIMe)Cl]$	**1d**	0.29	1.7	171	587
$[Ir^{III}(oep)(IMe)_2]^+$	**2c**	0.41	2.7	152	368
$[Ir^{III}(oep)(BIMe)_2]^+$	**2d**	0.66	3.6	183	276
$[Ir^{III}(oep)(I^iPr)_2]^+$	**2e**	0.03	1.9	16	526
$[Ir^{III}(F_{20}tpp)(IMe)_2]^{+c}$	**2f**	0.08	0.5	160	1998
$[Ir^{III}(oep)(CNPhOMe)_2]^+$	**3**	6.40	124.7	52	8
$[Ir^{III}(oep)(py)_2]^+$	**4**	12.30	55.3	222	16

^{a} Radiative decay rate constant determined by $k_r = \Phi_{em}/\tau$. ^{b} Nonradiative decay rate constant determined by $k_{nr} = (1 - \Phi_{em})/\tau$. ^{c} Data in CH$_2Cl_2$.

[Ru^{II}(oep)(CO)] reported by Bogoeva and co-workers.[40] Complex **2c** accumulates preferentially in cellular ER and somewhat in mitochondria as shown by the confocal laser microscopy images in the co-staining experiments, which could account for the subsequent induction of ER stress and mitochondrial membrane depolarization by this complex.

Incorporation of bis-NHC ligands to iridium(III) porphyrin also endows the complexes to display remarkable singlet oxygen production capability. Complex **2c** (with octaethylporphyrin) has the highest Φ_{so} compared to **2a** (with *meso*-tetratolylporphyrin) and other iridium(III) complexes ([Ir^{III}(corrole)(pyridine)$_2$] and [Ir^{III}(ttp)(aza-BODIPY)]) without bis-NHC ligands; it exhibits potent cytotoxicity with an IC$_{50}$ value in the nano-molar range and triggers the generation of ROS upon visible light irradiation. The photo-induced production of ROS (*e.g.*, $^1O_2$) was found to lead to oxidation of sulfur-containing residues of peptides, which is presumably a cytotoxic, protein-damaging mechanism. The photo-cytotoxic effects led to induction of apoptotic cell death and inhibition of angiogenesis. The *in vivo* photo-induced antitumor effect of **2c** was demonstrated in a mouse xenograft model of human lung cancer. Overall, given the synergetic anticancer properties of the prototype bis-NHC iridium(III) porphyrin complexes in the dark and upon light activation as well as the flexibility in derivatization of NHC ligand, cationic [Ir^{III}(por)(NHC)$_n$]$^+$ (H$_2$por = porphyrin; n = 1 or 2) complexes have great potential for development as a new class of photo-activated anticancer agents.

Conclusions

We synthesized a panel of luminescent ruffled iridium(III) porphyrin complexes bearing mono- and bis-NHC ligands, four of which were structurally characterized by X-ray crystallography. The unique photophysical properties resulting from the coordination of NHC ligands, including split Soret bands, broadened and redshifted absorption and emission spectra and substantially reduced emission quantum yield and lifetime, were investigated by spectroscopic and theoretical means and discussed. In spite of the low triplet-state energy, which limits their use as a photoredox mediator, the bis-NHC complexes are versatile photochemical singlet oxygen generators that can efficiently catalyze the photoinduced aerobic oxidation of secondary amines and arylboronic acids. In addition, the bis-NHC complexes are stable in physiological conditions and exhibit potent cytotoxicity and photocytotoxicity, presumably *via* the generation of ROS, against a panel of cancer cell lines, and one was demonstrated to have significant inhibitory effects against tumor growth in a nude mouse model.

Author contributions

Chi-Ming Che designed and initiated this research project. Chun-Nam Lok designed the biological experiments. Tsz-Lung Lam synthesized and characterized all complexes in this work, performed the spectroscopic and electrochemical measurements and carried out the photocatalytic reactions. Tsz-Lung Lam, Chun-Nam Lok, and Chi-Ming Che wrote the manuscript. Ka-Chung Tong and Wai-Lun Kwong carried out the biological experiments. Chen Yang was responsible for X-ray crystal structure determinations and assisted the time-resolved spectroscopic measurements. Ming-De Li and David Lee Phillips carried out the resonance Raman spectroscopic measurements. Xianguo Guan, Vanessa Kar-Yan Lo, and Sharon Lai-Fung Chan were responsible for the DFT/TDDFT calculations on UV-vis absorption spectra as well as resonance Raman spectra and the associated vibrational mode assignments. All authors reviewed the manuscript.

Conflicts of interest

There are no conflicts to declare.

Acknowledgements

Notes and references

1 Selected reviews: (*a*) *N-Heterocyclic Carbenes in Synthesis*, ed. S. P. Nolan, Wiley-VCH, New York, 2006; (*b*) *N-Heterocyclic Carbenes in Transition Metal Catalysis*, ed. F. Glorius, Springer-Verlag, Berlin, Heidelberg, 2007, vol. 21; (*c*) S. Díez-González, N. Marion and S. P. Nolan, *Chem. Rev.*, 2009, **109**, 3612–3676; (*d*) L.-A. Schaper, S. J. Hock, W. A. Herrmann and F. E. Kühn, *Angew. Chem., Int. Ed.*, 2013, **52**, 270–289; (*e*) A. Nasr, A. Winkler and M. Tamm, *Coord. Chem. Rev.*, 2016, **316**, 68–124; (*f*) D. Janssen-Müller, C. Schlepphorst and F. Glorius, *Chem. Soc. Rev.*, 2017, **46**, 4845–4854.

2 Selected reviews: (*a*) L. Meres and M. Albrecht, *Chem. Soc. Rev.*, 2010, **39**, 1903–1912; (*b*) R. Visbal and M. C. Gimeno, *Chem. Soc. Rev.*, 2014, **43**, 3551–3574; (*c*) M. Elie, J.-L. Renaud and S. Gaillard, *Polyhedron*, 2018, **140**, 158–168.

3 Selected reviews: (*a*) K. M. Hindi, M. J. Panzner, C. A. Tessier, C. L. Cannon and W. J. Youngs, *Chem. Rev.*, 2009, **109**, 3859–3884; (*b*) M.-L. Teyssot, A.-S. Jarrousse, M. Manin, A. Chevry, S. Roche, F. Norre, C. Beaudoin, L. Morel, D. Boyer, R. Mahiou and A. Gautier, *Dalton Trans.*, 2009, 6894–6902; (*c*) L. Oehninger, R. Rubbiani and I. Ott, *Dalton Trans.*, 2013, **42**, 3269–3284; (*d*) W. Liu and R. Gust, *Chem. Soc. Rev.*, 2013, **42**, 755–773; (*e*) F. Cisnetti and A. Gautier, *Angew. Chem., Int. Ed.*, 2013, **52**, 11976–11978; (*f*) C. Hu, X. Li, W. Wang, R. Zhang and L. Deng, *Curr. Med. Chem.*, 2014, **21**, 1220–1230; (*g*) W. Liu and R. Gust, *Coord. Chem. Rev.*, 2016, **329**, 191–213.

4 Selected reviews: (*a*) P. L. Arnold and I. J. Casely, *Chem. Rev.*, 2009, **109**, 3599–3611; (*b*) H. Jacobsen, A. Correa, A. Poater, C. Costabile and L. Cavallo, *Coord. Chem. Rev.*, 2009, **253**, 687–703; (*c*) J. C. Y. Lin, R. T. W. Huang, C. S. Lee,

A. Bhattacharyya, W. S. Hwang and I. J. B. Lin, *Chem. Rev.*, 2009, **109**, 3561–3598; (*d*) P. G. Edwards and F. E. Hahn, *Dalton Trans.*, 2011, **40**, 10278–10288; (*e*) S. J. Hock, L.-A. Schaper, W. A. Herrmann and F. E. Kühn, *Chem. Soc. Rev.*, 2013, **42**, 5073–5089; (*f*) C. Fliedel, G. Schnee, T. Avilés and S. Dagorne, *Coord. Chem. Rev.*, 2014, **275**, 63–86; (*g*) S. Bellemin-Laponnaz and S. Dagorne, *Chem. Rev.*, 2014, **114**, 8747–8774; (*h*) V. Charra, P. de Friémont and P. Braunstein, *Coord. Chem. Rev.*, 2017, **341**, 53–176.

5 (*a*) M. Albrecht, P. Maji, C. Häusl, A. Monney and H. Müller-Bunz, *Inorg. Chim. Acta*, 2012, **380**, 90–95; (*b*) J. Olguin, H. Müllen-Bunz and M. Albrecht, *Chem. Commun.*, 2014, **50**, 3488–3490.

6 B. J. Anding, A. Ellern and L. K. Woo, *Organometallics*, 2014, **33**, 2219–2229.

7 K.-H. Chan, X. Guan, V. K.-Y. Lo and C.-M. Che, *Angew. Chem., Int. Ed.*, 2014, **53**, 2982–2987.

8 (*a*) C. M. Drain, C. Kirmaier, C. J. Medforth, D. J. Nurco, K. M. Smith and D. Holten, *J. Phys. Chem.*, 1996, **100**, 11984–11993; (*b*) J. A. Shelnutt, X.-Z. Song, J.-G. Ma, S.-L. Jia, W. Jentzen and C. J. Medforth, *Chem. Soc. Rev.*, 1998, **27**, 31–42; (*c*) A. B. Parusel, T. Wondimagegn and A. Ghosh, *J. Am. Chem. Soc.*, 2000, **122**, 6371–6374; (*d*) R. E. Haddad, S. Gazeau, J. Pecaut, J.-C. Marchon, C. J. Medforth and J. A. Shelnutt, *J. Am. Chem. Soc.*, 2003, **125**, 1253–1268; (*e*) A. Y. Lebedev, M. A. Filatov, A. V. Cheprakov and S. A. Vinogradov, *J. Phys. Chem. A*, 2008, **112**, 7723–7733; (*f*) F. Nifiatis, W. Su, J. E. Haley, J. E. Slagle and T. M. Copper, *J. Phys. Chem. A*, 2011, **115**, 13764–13772; (*g*) M. O. Senge, S. A. MacGowan and J. M. O'Brien, *Chem. Commun.*, 2015, **51**, 17031–17063.

9 (*a*) C. J. Medforth, M. O. Senge, K. M. Smith, L. D. Sparks and J. A. Shelnutt, *J. Am. Chem. Soc.*, 1992, **114**, 9859–9869; (*b*) K. M. Kadish, M. Lin, E. Van Caemelbecke, G. De Stefano, C. J. Medforth, D. J. Nurco, N. Y. Nelson, B. Krattinger, C. M. Muzzi, L. Jaquinod, Y. Xu, D. C. Shyr, K. M. Smith and J. A. Shelnutt, *Inorg. Chem.*, 2002, **41**, 6673–6687; (*c*) A. Rosa, G. Ricciardi, E. J. Baerends, M. Zimin, M. A. J. Rodgers, S. Matsumoto and N. Ono, *Inorg. Chem.*, 2005, **44**, 6609–6622; (*d*) N. Grover, M. Sankar, Y. Song and K. M. Kadish, *Inorg. Chem.*, 2016, **55**, 584–597; (*e*) J. Schindler, S. Kupfer, A. A. Ryan, K. J. Flanagan, M. O. Senge and B. Dietzek, *Coord. Chem. Rev.*, 2018, **360**, 1–16.

10 (*a*) F. D'Souza, M. E. Zandler, P. Tagliatesta, Z. Ou, J. Shao, E. V. Caemelbeck and K. M. Kadish, *Inorg. Chem.*, 1998, **37**, 4567–4572; (*b*) B. Röder, M. Büchner, I. Rückmann and M. O. Senge, *Photochem. Photobiol. Sci.*, 2010, **9**, 1152–1158.

11 (*a*) R. Guilard, K. Perié, J.-M. Barbe, D. J. Nurco, K. M. Smith, E. Van Caemelbecke and K. M. Kadish, *Inorg. Chem.*, 1998, **37**, 973–981; (*b*) I. Akira and N. Mikio, *Chem. Lett.*, 2005, **34**, 1046–1047l; (*c*) A. Ikezaki and M. Nakamura, *J. Porphyrins Phthalocyanines*, 2016, **20**, 1–13.

12 (*a*) T. Sakai, Y. Ohgo, A. Hoshino, T. Ikeue, T. Saitoh, M. Takahashi and M. Nakamura, *Inorg. Chem.*, 2004, **43**, 5034–5043; (*b*) M. Nakamura, *Coord. Chem. Rev.*, 2006, **250**, 2271–2294; (*c*) A. Tozuka, A. Ikezaki, M. Taniguchi and

M. Nakamura, *Inorg. Chem.*, 2010, **49**, 10400–10408; (*d*) M. Li, A. G. Oliver, T. J. Neal, C. E. Schulz and W. R. Scheidt, *J. Porphyrins Phthalocyanines*, 2013, **17**, 118–124; (*e*) D. Sahoo and S. P. Rath, *Chem. Commun.*, 2015, **51**, 16790–16793.

13 (*a*) R. Salzmann, C. J. Ziegler, N. Godbout, M. T. McMahon, K. S. Suslick and E. Oldfield, *J. Am. Chem. Soc.*, 1998, **120**, 11323–11334; (*b*) Z. Yao, C. E. Schulz, N. Zhan and J. Li, *Inorg. Chem.*, 2017, **56**, 12615–12624.

14 M. Gouterman, in *The Porphyrins*, ed. D. Dolphin, Academic Press, New York, 1978, vol. 3, pp. 1–165.

15 (*a*) L. K. Hanson, M. Gouterman and J. C. Hanson, *J. Am. Chem. Soc.*, 1973, **95**, 4822–4829; (*b*) A. Antipas, J. W. Buchler, M. Gouterman and P. D. Smith, *J. Am. Chem. Soc.*, 1978, **100**, 3015–3024; (*c*) A. Antipas, J. W. Buchler, M. Gouterman and P. D. Smith, *J. Am. Chem. Soc.*, 1980, **102**, 198–207; (*d*) L. M. A. Levine and D. Holten, *J. Phys. Chem.*, 1998, **92**, 714–720.

16 (*a*) K. Koren, S. M. Borisov, R. Saf and I. Klimant, *Eur. J. Inorg. Chem.*, 2011, 1531–1534; (*b*) K. Koren, R. I. Dmitriev, S. M. Borisov, D. B. Papkovsky and I. Klimant, *ChemBioChem*, 2012, **13**, 1184–1190; (*c*) B.-B. Wang, H. Zho, J. Mack, P. Majumdar, T. Nyokong, K. S. Chan and Z. Shen, *J. Porphyrins Phthalocyanines*, 2015, **19**, 973–982; (*d*) J. Zhou, L. Gai, Z. Zhou, J. Mack, K. Xu, J. Zhao, H. Qiu, K. S. Chan and Z. Shen, *RSC Adv.*, 2016, **6**, 72115–72120.

17 Selected examples of coordinating NHC ligand to iridium metal center *via* transmetallation of $[Ag(NHC)_2]^+$ complexes: (*a*) S. Burling, M. F. Mahon, S. P. Reade and M. K. Whittlesey, *Organometallics*, 2006, **25**, 3761–3767; (*b*) L. N. Appelhans, C. D. Incarvito and R. H. Crabtree, *J. Organomet. Chem.*, 2008, **693**, 2761–2766; (*c*) U. Hintermair, U. Englert and W. Leitner, *Organometallics*, 2011, **30**, 3726–3731.

18 C.-M. Che and W.-Y. Yu, *Pure Appl. Chem.*, 1999, **71**, 281–288. Oxidation state marker band of [Ir^{III}(tmp)Cl(CO)]: $\nu = 1022$ cm^{-1}; [Ir^{III}(F$_{20}$tpp)Cl(CO)]: $\nu = 1026$ cm^{-1}; [Ir^{III}(ttp) Cl(CO)]: $\nu = 1017$ cm^{-1}; [Ir^{III}(oep)Cl(CO)]: $\nu = 1022$ cm^{-1}.

19 (*a*) X. Song and K. S. Chan, *Organometallics*, 2007, **26**, 965–970; (*b*) C. W. Cheung and K. S. Chan, *Organometallics*, 2008, **27**, 3043–3055; (*c*) C. W. Cheung and K. S. Chan, *Organometallics*, 2011, **30**, 4269–4283.

20 Selected examples: (*a*) J. M. Meredith, R. Robinson Jr, K. I. Goldberg, W. Kaminsky and D. M. Heinekeym, *Organometallics*, 2012, **31**, 1879–1887; (*b*) M. C. Lehman, P. D. Boyle, R. D. Sommer and E. A. Ison, *Organometallics*, 2014, **33**, 5081–5084; (*c*) S. Sabater, M. Baya and J. A. Mata, *Organometallics*, 2014, **33**, 6830–6839; (*d*) L. Rubio-Pérez, M. Iglesias, J. Munárriz, V. Polo, V. Passarelli, J. J. Pérez-Torrente and L. A. Oro, *Chem. Sci.*, 2017, **8**, 4811–4822.

21 C. J. Medforth, in *The Porphyrin Handbook*, ed. K. M. Kadish, K. M. Smith and R. Guilard, Academic Press, Boston, 2000, vol. 5, pp. 1–80.

22 (*a*) J. R. Polam, T. K. Shokhireva, K. Raffii, U. Simonis and F. A. Walker, *Inorg. Chim. Acta*, 1997, **263**, 109–117; (*b*) C. J. Medforth, C. M. Muzzi, K. M. Smith, R. J. Abraham, J. D. Hobbs and J. A. Shelnutt, *J. Chem. Soc., Chem.*

Commun., 1994, 1843–1844; (*c*) C. J. Medforth, R. E. Haddad, C. M. Muzzi, N. R. Dooley, L. Jaquinod, D. C. Shyr, D. J. Nurco, M. M. Olmstead, K. M. Smith, J.-G. Ma and J. A. Shelnutt, *Inorg. Chem.*, 2003, **42**, 2227–2241.

23 (*a*) H. Scheer and J. J. Katz, in *Porphyrins and Metalloporphyrins*, ed. K. M. Smith, Elsevier, Amsterdam, 1975, pp. 399–524; (*b*) Y. Li, J.-S. Huang, G.-B. Xu, N. Zhu, Z.-Y. Zhou, C.-M. Che and K.-Y. Wong, *Chem.–Eur. J.*, 2004, **10**, 3486–3502; (*c*) C.-M. Che, C.-M. Ho and J.-S. Huang, *Coord. Chem. Rev.*, 2007, **251**, 2145–2166.

24 C. Swistak, J.-L. Cornillon, J. E. Anderson and K. M. Kadish, *Organometallics*, 1987, **6**, 2146–2150.

25 (*a*) R. H. Felton, in *The Porphyrins*, ed. D. Dolphin, Academic Press, San Diego, 1978, vol. 5, pp. 53–126; (*b*) P. Chen, O. S. Finikova, Z. Ou, S. A. Vinogradow and K. M. Kadish, *Inorg. Chem.*, 2012, **51**, 6200–6210.

26 C.-J. Liu, W.-Y. Yu, S.-M. Peng, T. C. W. Mak and C.-M. Che, *J. Chem. Soc., Dalton Trans.*, 1998, 1805–1812.

27 R. Horvath and K. C. Gordon, *Coord. Chem. Rev.*, 2010, **254**, 2505–2518.

28 (*a*) S.-W. Lai, Y. J. Hou, C.-M. Che, H.-L. Pang, K.-Y. Wong, C. K. Chang and N. Zhu, *Inorg. Chem.*, 2004, **43**, 3724–3732; (*b*) D. B. Papkovsky and T. C. O'Riordan, *J. Fluoresc.*, 2005, **15**, 569–584; (*c*) W.-P. To, Y. Liu, T.-C. Lau and C.-M. Che, *Chem.–Eur. J.*, 2013, **19**, 5654–5664.

29 W. Sinha, L. Ravotto, P. Ceroni and S. Kar, *Dalton Trans.*, 2015, **44**, 17767–17773.

30 F. Wilkinson, W. P. Helman and A. B. Ross, *J. Phys. Chem. Ref. Data*, 1993, **22**, 113–262.

31 (*a*) C.-M. Che, R. W.-Y. Sun, W.-Y. Yu, C.-B. Ko, N.-Y. Zhu and H. Z. Sun, *Chem. Commun.*, 2003, 1718–1719; (*b*) C.-T. Lum, Z. F. Yang, H.-Y. Li, R. W.-Y. Sun, S.-T. Fan, R. T.-P. Poon, M. C.-M. Lin, C.-M. Che and H.-F. Kung, *Int. J. Cancer*, 2006, **118**, 1527–1538; (*c*) Y. Wang, Q. Y. He, R. W.-Y. Sun, C.-M. Che and J.-F. Chiu, *Cancer Res.*, 2005, **65**, 11553–11564; (*d*) R. W.-Y. Sun, C. K.-L. Li, D.-L. Ma, J. J. Yan, C.-N. Lok, C.-H. Leung, N. Zhu and C.-M. Che, *Chem.–Eur. J.*, 2010, **16**, 3097–3113; (*e*) R. W.-Y. Sun, A. L.-F. Chow, X.-H. Li, J. J. Yan, S. S.-Y. Chui and C.-M. Che, *Chem. Sci.*, 2011, **2**, 728–736; (*f*) C.-T. Lum, R. W.-Y. Sun, T. T. Zou and C.-M. Che, *Chem. Sci.*, 2014, **5**, 1579–1584; (*g*) C. Y. Chung, S. K. Fung, K.-C. Tong, P.-K. Wan, C.-N. Lok, Y. Huang, T. Chen and C.-M. Che, *Chem. Sci.*, 2017, **8**, 1942–1953; (*h*) S. K. Fung, T. Zou, B. Cao, P.-Y. Lee, E. Y. M. Fung, D. Hu, C.-N. Lok and C.-M. Che, *Angew. Chem., Int. Ed.*, 2017, **56**, 3892–3896.

32 T. T. Zou, C.-N. Lok, Y.-M. Fung and C.-M. Che, *Chem. Commun.*, 2013, **49**, 5423–5425.

33 B. J. Anding, J. Brgoch, G. J. Miller and L. K. Woo, *Organometallics*, 2012, **31**, 5586–5590.

34 L. J. Boucher, *Coord. Chem. Rev.*, 1972, **7**, 289–329.

35 (*a*) M. C. DeRosa and R. J. Crutchley, *Coord. Chem. Rev.*, 2002, **233–234**, 351–371; (*b*) H.-G. Jeong and M.-S. Choi, *Isr. J. Chem.*, 2016, **56**, 110–118; (*c*) M. Soll, K. Sudhakar, N. Fridman, A. Müller, B. Röder and Z. Gross, *Org. Lett.*, 2016, **18**, 5840–5843.

36 (*a*) G. S. D. Tyler, Y.-Y. Huang and H. R. Michael, in *Handbook of Porphyrin Science*, ed. K. M. Kadish, K. M. Smith and R. Guilard, World Scientific, London, 2014, vol. 27, pp. 255–301; (*b*) S. Sunaina, A. Aggarwal, N. V. D. K. Bhupathiraju, G. Arianna, K. Tiwari and C. M. Drain, *Chem. Rev.*, 2015, **115**, 10261–10306.

37 Y.-Z. Chen, Z. U. Wang, H. Wang, J. Lu, S.-H. Yu and H.-L. Jiang, *J. Am. Chem. Soc.*, 2017, **139**, 2035–2044.

38 (*a*) L. Flamigni, A. Barbieri, C. Sabatini, B. Ventura and F. Barigelletti, *Top. Curr. Chem.*, 2007, **281**, 143–203; (*b*) Y. You and W. Nam, *Chem. Soc. Rev.*, 2012, **41**, 7061–7084.

39 J. J. Yan, A. L.-F. Chow, C.-H. Leung, R. W.-Y. Sun, D.-L. Ma and C.-M. Che, *Chem. Commun.*, 2010, **46**, 3893–3895.

40 V. Bogoeva, M. Siksjø, K. G. Sæterbø, T. B. Melø, A. Bjørkøy, M. Lindgren and O. A. Gederaas, *Photodiagn. Photodyn. Ther.*, 2016, **14**, 9–17.